Identifying the provenance and quantifying the contribution of dust sources in EPICA Dronning Maud Land ice core (Antarctica) over the last deglaciation (7-27 kyr BP): a high-resolution, quantitative record from a new Rare Earth Element mixing model

Aubry Vanderstraeten[1,2], Nadine Mattielli[1], Goulven G. Laruelle[3], Stefania Gili[4], Aloys Bory[2], Paolo Gabrielli[5], Sibylle Boxho[1], Jean-Louis Tison[6] and Steeve Bonneville[3*]

[1] Laboratoire G-Time, Département Géosciences, Environnement et Société (DGES), Université Libre de Bruxelles (ULB), Av. F. Roosevelt, 50 (CP 160/02), Brussels, 1050, Belgium.

[2] Laboratoire d'Océanologie et de Géosciences UMR 8187 – LOG, Univ. Lille, CNRS, Univ. Littoral Côte d'Opale, IRD, F-59000 Lille, France

[3] Biogéochimie et Modélisation du Système Terre, Département Géosciences, Environnement et Société (DGES), Université Libre de Bruxelles (ULB), Brussels, 1050, Belgium.

[4] Department of Geosciences, Princeton University, Princeton, NJ 08544, United States of America.

[5] Italian Glaciological Committee, c/o University of Turin, Turin, Italy

[6] Laboratoire de Glaciologie, Département Géosciences, Environnement et Société (DGES), Université Libre de Bruxelles (ULB), Av. F. Roosevelt, 50 (CP 160/02), Brussels, 1050, Belgium.

*corresponding author

Abstract

Antarctic ice cores have revealed the interplay between dust and climate in the Southern Hemisphere. Yet, so far, no continuous record of dust provenance has been established through the last deglaciation. Here, using a new database of 207 Rare Earth Element (REE) patterns measured in dust and sediments/soils from well-known potential source areas (PSA) of the Southern Hemisphere, we developed a statistical model combining those inputs to provide the best fit to the REE patterns measured in EPICA Dronning Maud Land (EDML) ice core (E. Antarctica). Out of 398 samples measured in the EDML core, 386 samples have been un-mixed with statistical significance. Combined with the total atmospheric deposition, we quantified the dust flux from each PSA to EDML between 7-27 kyr BP. Our results reveal that the dust composition was relatively uniform up until 14.5 kyr BP despite a large drop in atmospheric deposition at ~18 kyr with a large contribution from Patagonia yielding ~68% of total dust deposition. The remaining dust was supplied from Australia (14-15%), Southern Africa (~9%), New Zealand (~3-4%) and Puna-Altiplano (~2-3%). The most striking change occurred ~14.5 kyr BP when Patagonia dropped below 50% on average while low-latitude PSA increased their contributions to 21-23% for Southern Africa, 13-21% for Australia and ~4-10% for Puna-Altiplano. We argue that this shift is linked to long-lasting changes in the hydrology of Patagonian rivers and to sudden acceleration of the submersion of Patagonian shelf at 14.5 kyr BP, highlighting a relationship between dust composition and eustatic sea level. Early Holocene dust composition is highly variable, with Patagonian contribution being still prevalent, at ~50% on average. Provided a good coverage of local and distal PSA, our statistical model based on REE pattern offers a straightforward and cost-effective method to trace dust source in ice cores.

46 **Graphical abstract:**

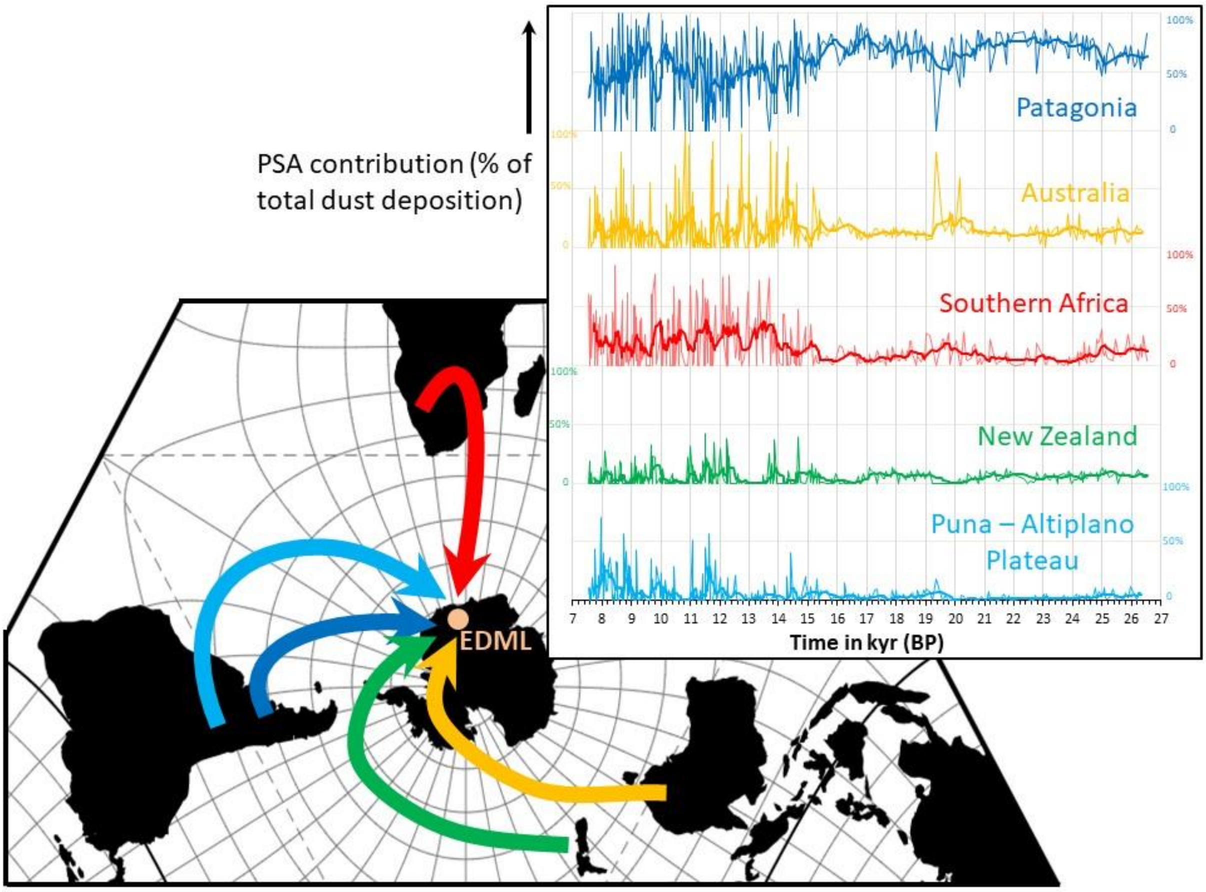

47

48

1. Introduction

Ice cores collected in Antarctica are invaluable, direct and highly-resolved archives of the past atmosphere and of the Earth's climate (Lambert et al., 2008). Together with deep-sea sediment drillings in the Southern Ocean, Antarctic ice cores have revealed the close connection between dust deposition rates and export productivity, possibly relating the emergence of deep glaciations with dust-laden atmosphere in the Southern Hemisphere (SH) via the impact of dust on phytoplankton growth in the HNLC (High Nitrate Low Chlorophyll) waters of the Southern Ocean (Martínez-García et al., 2014). Using Antarctic ice cores, Lambert et al., (2008) suggested that the location of the dust source regions and the lifetime of dust in the atmosphere are the main factors controlling the high dust flux during glacial periods. As such, the stimulation of ocean surface biological activity through the enhanced delivery of Fe by dust during glacial times may have lowered the atmospheric pCO_2 by ~20 ppmv (Lambert et al., 2015), which represents about a quarter to a third of the difference in pCO_2 between interglacial and glacial periods. More recently, Lambert et al., (2021) confirmed that the Southern Ocean was the most sensitive oceanic area to iron fertilization, with the Atlantic and Pacific sectors accounting for ~57% of the total CO_2 reduction from iron fertilization globally. Yet, those estimates of pCO_2 drawdown suffer from large uncertainties stemming from the lack of knowledge about dust emission from each individual PSA during the last glacial-interglacial transition. Indeed, Patagonian dust and Southern African dust for instance have distinct iron contents (Qu, 2016) and iron solubility in general has been shown to vary according to the weathering intensity in topsoil source (Shi et al., 2011). Quantifying the contribution of each PSA in aeolian deposits such as Antarctic ice cores is thus instrumental not only to reconstruct paleoclimates in the SH continental source regions but also to improve estimates of the dust climate feedback through iron fertilization. Establishing a record of dust provenance would also help to better constrain shifts in the position and strength of the SH westerly winds, which is key to our understanding of atmospheric and oceanic circulation changes during the last glacial cycle (Engelbrecht et al., 2019). As Antarctic ice cores accumulate continuously, are well dated and receive dust from long-distance transport (especially drill-site located inland at high altitude), they provide a valuable record of dust deposition. Recently, Coppo et al., (2022) estimated the average provenance of dust reaching East Antarctica plateau over the LGM and Holocene using isotopic fingerprint. Yet, to our best knowledge, no quantitative, high-resolution (centennial to decade) and continuous provenance record of dust source apportionment has been established from Antarctic ice cores throughout the Last Glaciation Interglacial Transition (LGIT).

The favored method to trace dust consists in matching the geochemical fingerprint of PSA with those of dust preserved in eolian deposits. Isotopic ratios of Nd, Sr or Pb and the pattern of Rare Earth Elements (REE) concentrations (Marx et al., 2005) have proved to be the most reliable indicators for provenance purposes (Grousset and Biscaye, 2005). Using isotopic signatures, Patagonia (PAT) was identified as the main supplier of dust to Antarctica during the Last Glacial Maximum (LGM) (Grousset et al., 1992; Basile et al., 1997; Gaiero, 2007; Gaiero et al., 2013; Gili et al., 2017), yet its specific contribution could not be quantified. It is also still unclear which were the other PSA supplying dust to Antarctica during the LGM. Several PSA have been proposed, such as Australia (De Deckker et al., 2010), New Zealand (Neff and Bertler, 2015; Koffman et al., 2021), and other Southern South American sources such as Southern Central West Argentina or Puna-Altiplano Plateaus (Gili et al., 2017; Gaiero, 2007; Gaiero et al., 2004). As for the interglacial periods, because of the drop in atmospheric deposition in Antarctica, obtaining reliable isotopic fingerprint requires a much larger amount of ice - up to 60-90 cm of ice core per measurement (Delmonte et al., 2017) which reduces the temporal resolution of the record. Independently of analytical limitations, interpreting dust isotopic fingerprints in terms of provenance is complex as most PSA have overlapping isotopic ‘domains’ (Gaiero et al., 2004; Gili et al., 2017; Delmonte et al., 2017; Delmonte et al., 2020). The matter is further complexified by the mixing of dust coming from multiple sources during atmospheric transport and déposition.

To overcome those limitations, the use of REE patterns to trace dust is promising: REE analyses are less time-consuming, sensitive and precise and can thus be done on a lesser amount of dust compared to isotopes, allowing for a higher (spatio)-temporal resolution. Gabrielli et al., (2010) and Wegner et al., (2012) reached a multi-decadal temporal resolution in their analyses of dust REE concentrations in EPICA Dronning Maud Land (EDML) and EPICA Dome C (EDC) ice cores. Yet, those studies could not decipher the provenance of dust from their REE pattern. Here, we developed the first apportionment model based on REE pattern fitting that is able to disentangle multiple dust inputs from a large number of dust sources across the Southern Hemisphere. We applied this model to the REE pattern dataset from (Wegner et al., 2012) in order to provide the first quantitative, continuous, high-resolution reconstruction of dust provenance at EDML, East Antarctica throughout the Last Glacial Interglacial Transition (LGIT).

2. Statistical analysis of EDML REE patterns

The EDML REE dataset, comprising 398 samples from (*21* - data are available at https://doi.org/10.1594/PANGAEA.756834), covers the last glacial-interglacial transition from 26.568 kyr to 7.554 kyr at an average temporal resolution of ~48 yr (varying from 18 to 171 yr) between adjacent samples. To identify and quantify dust source contributions to E. Antarctica, we developed a method based on a numerical algorithm that solves a set of linear equations using a least-squares method while only allowing positive coefficients in order to provide the best fit of the dust REE patterns measured in EDML by combining REE patterns from well-known PSAs across the Southern Hemisphere. The details of our approach are summarized below.

Out of 398 samples from the original EDML REE dataset, two samples were removed as they missed concentration data for one or more of the 14 different REE required for our model. The remaining 396 EDML REE samples were normalized to the Upper Continental Crust (UCC) composition (Rudnick and Gao, 2003) and by an element-specific correction factor (*cf* - Table S1) resulting from the analytical procedure detailed in (Gabrielli et al., 2010). Those elemental-specific *cf* values account for the fact that the REE concentrations of EDML dust were measured via an acid-leaching method (Wegner et al., 2012) implying analysis of samples containing partially dissolved dust particles that may not be fully atomized in the plasma (and detected) by Inductively Coupled Plasma Sector Field Mass Spectrometry. Thus, in order to transform those ‘partial’ dissolution REE concentrations into total bulk REE concentrations allowing for comparison with REE patterns from PSA (which are measured after full acid digestion), we applied an elemental-specific correction factors (*cf* , Table S1) :

$$cf_i = \frac{[REE]i\ full\ digestion}{[REE]i\ acid{-}leaching} \qquad \text{(Eq. 1)}$$

where $[REE]_i$ denotes the concentration of a given REE *i* measured via a full digestion and in partial acid-leaching method for glacial dust in EDC ice core (Gabrielli et al., 2010). As the methodology applied at EDC and EDML sites is the same, and that dust from those two sites were shown to have similar dust composition (*25*; *26*), we applied the elemental-specific cf_i derived from EDC dust to the EDML dataset ($Dust_i$ in ng/L) from (Wegner et al., 2012) and define the normalized concentration of a given REE *i* in the Dust Ice Core samples (DIC_i) as follows:

$$DIC_i = \frac{Dust_i \times cf_i}{UCC_i} \qquad \text{(Eq. 2)}$$

with UCC_i, the Upper Crust Concentration for the element *i*. Depending on the element, the *cf* values ranges from 1.621 to 2.801 (Gabrielli et al., 2010) are presented in Table S1 (as well as their standard deviation values - 1SD).

For the PSA, we assembled a large database consisting of 207 REE patterns spanning across well-known PSAs of the SH comprising: Patagonia (PAT - 39 Dust Source -DS-), Central Western Argentina (CWA - 5 DS), Puna-Altiplano Plateau (PAP - 14 DS), Southern Africa (SAF - 17 DS), Australia (AUS - 107 DS, focused mostly in S-E) and New Zealand (NZ - 25 DS) (see Fig. S1 for maps; Table S2 for localization of DS, physical characteristics, REE chemical composition; Fig S2 for REE patterns). In addition, as for DIC, all DS are normalized to UCC (Rudnick and Gao, 2003). The idea of the database is to sample the geochemical variability of atmospheric dust within each PSA, thus we prioritized the local mineral dust or the fine fraction (<5 µm) of loess, sediment or soils, however when unavailable, coarser sediment/topsoil samples (<63 µm and <90 µm for South Altiplano and Australia, respectively) were incorporated into the DS. We also analyzed REE content of the fine fraction (<5 µm) in samples collected in Southern Africa especially from the dry riverbed sediments from Namib desert coast (see Supplementary Information and Gili et al., 2022). Antarctic dust is not considered as dust source in our model as (Wegner et al., 2012) has shown that Antarctic dust sources (mostly from Dry Valleys) have a distinctive enrichment in light REE that is not consistent with the REE patterns of EDML dust. Model runs with Antarctic sources including DS from the Dry Valley region (Diaz et al., 2020) and cryoconites collected near the Sør Rondane Mountains confirmed this observation, showing very low inputs (<5% in contribution in 7 samples – data not shown). Local sources of dust generate coarser grain size distribution with a significant amount of 5-10 µm particles and a poor size sorting as observed in Talos Dome ice core (Delmonte et al., 2010) and in Berkner Island surface snow (Bory et al., 2010). The latter features are absent in EDML grain size distribution (Wegner et al., 2015). Indeed, the grain size mode in EDML (2892 m.a.s.l.) range between 1.8 and 2.6 µm and is similar to EPICA Dome C dust size which is known to receive only atmospheric deposition from long-range intercontinental transport (Wegner et al., 2015). All in all, we posit that local and Antarctic dust do not influence significantly the REE fingerprint in EDML.

The fitting of dust REE pattern can be defined as a constrained least squares problem where the coefficients (*i.e*., the respective contributions of each DS - i.e., $CDS^{1\ldots207}$- in a given DIC sample) are not allowed to be negative (*lsqnonneg* function from Matlab). Thus, the goal of our fitting approach is to minimize the following expression:

$$\left\| \begin{bmatrix} DS^{1}_{La} & \cdots & DS^{207}_{La} \\ \vdots & \ddots & \vdots \\ DS^{1}_{Lu} & \cdots & DS^{207}_{Lu} \end{bmatrix} \times \begin{pmatrix} CDS^{1} \\ \vdots \\ CDS^{207} \end{pmatrix} - \begin{pmatrix} DIC_{La} \\ \vdots \\ DIC_{Lu} \end{pmatrix} \right\|_2^2 \qquad \text{(Eq. 3)}$$

That is, the ‘input’ matrix (14 rows × 207 columns) formed by the 14 UCC-normalized REE concentrations of the 207 DS is multiplied by a vector of 207 components (*i.e*., $CDS^{1\ldots207}$), which corresponds to the contributions of each DS to match the vector represented by the 14 REE concentrations in a given dust ice core sample ($DIC_{La\text{-}Lu}$). The selected set of CDS values is the one that minimizes the difference between the product of the input matrix and the CDS vector on one hand, and the DIC vector on the other hand. As such in Eq. 3, only a fraction of the 207 DS participates to the fit of a given DIC, i.e., the DS with CDS value > 0 (the DS with CDS value equal to zero do not contribute to the fit).

To quantify the impact of uncertainties (from the DIC REE concentration analyses and from *cf* values) on the results of our model, we performed Monte Carlo (MC) simulations for each ice dust sample. The analytical uncertainty for $Dust_i$ concentration data from the acid-leaching method was quantified in (Dick et al., 2008) and amounts to a relative standard deviation ranging between 4.5 % and 7.8 % (1 RSD) depending on the considered REE element (Table S1). For each MC simulation, the algorithm randomly assigns a value of cf_i and $Dust_i$ following a normal distribution (function *normrnd* from Matlab) constrained by their respective analytic uncertainties. Then, for each MC simulation, the model calculates the best fit of CDS values to minimize Eq. 3 (Fig. S3). Cumulated over 5000 MC simulations, the results of CDS (% contributions) provides a probability density function per DS for each time step (Fig. S4). All the DS probability density function that belongs to a given PSA are then aggregated (*i.e.,* added) to form a probability density function per PSA. We then calculate the median of each PSA probability density functions to quantify the contribution of every PSA (in % contribution of total dust deposition) in each DIC sample (Fig. S4). In addition, to the contributions, we used the total dust influx to EDML via non-sea-salt Ca flux - $nssCa^{2+}$ in µg m^{-2} yr^{-1} from (Fischer et al., 2007) to derive the dust flux coming from each PSA to EDML (Fig. S5).

To evaluate the goodness of the selected fit to a given DIC vector (the 14 REE concentrations of dust ice core), we calculated the correlation coefficient (R) for each MC iteration. Cumulated over 5000 MC simulations per DIC sample, those R values form a distribution from which we use the median R value to evaluate the overall goodness of the selected fits proposed by our model (Fig S3 and S5). To know whether there is a statistically significant relationship between the selected fit and a given DIC and determine the lower limit of R value admissible in our statistical analysis, we calculated the t-statistic values considering the overall number of observation pairs (i.e., 14 in this case, so n=14):

$$t = \frac{R \times \sqrt{n-2}}{\sqrt{(1-R^2)}} \qquad \text{(Eq. 4)}$$

Subsequently, from the evolution of the corresponding p-value (two-tailed test, degree of freedom of 12) as a function of the value of R, we could determine that p-value <0.01 (99% confidence to reject the null hypothesis) corresponds to a R>0.67. In other words, when R>0.67, there is sufficient evidence to conclude that there is a significant linear relationship between the selected fit and the REE pattern of the "target" dust sample. Out of the 396 samples of the dataset, only 6 samples (at 8.556, 13.642, 14.056, 15.991, 19.456 and 24.017 kyr BP) failed this threshold and were removed from our provenance reconstruction. Overall, 92% of the fits we calculated had a median R values >0.8 with their respective DIC (Fig. S5B). In addition, 4 more samples (at 14.785, 14.809, 14.833 and 14.858 kyr BP) were removed as they were impacted by a large deposition of volcanic/ash materials evidenced by a peak in sulfate concentration (Wegner et al., 2012). As *lsqnonneg* routine uses an iterative algorithm to solve Eq. 3, we also tested the influence of initialization conditions (i.e., the order of DS in the database) on the output of the model (See Supplementary Information and Fig. S7). Those additional results show that our results were independent of the initialization conditions of the input REE database.

3. Results

The provenance of 386 samples could be determined with sufficient statistical confidence to reconstruct the dust provenance record during the last glacial-interglacial transition in EDML, from 26.568 to 7.554 kyr BP. Figures 1 and 2 (Table S3 for detailed values) present the contributions we obtained expressed in percentage and flux of each PSA in the Southern Hemisphere to the dust deposited at EDML during the last glacial-interglacial transition.

3.1. LGM (26.568 to ~18 kyr BP)

Patagonia is the foremost dust source with an average contribution of ~68% of total dust deposition over the LGM (Fig. 1). An average of 104 different DS (out of the 207 DS available) was selected to fit the dust deposition at EDML (Fig. S7). For PAT, our model points out a northern DS (41°19'S 69°31'W) located within a large closed-basin in the 'North Patagonian Massif Plateau' – a 10^5 km^2 basaltic plateau culminating at 1200 m. The secondary sources reaching EDML are, in decreasing order of importance: Australia (DS from Murray-Darling basins), SAF (mostly DS from Sua and Etosha pans) and NZ with, respectively, ~14%, 9% and 5 % of total deposition respectively. Despite the large number of DS involved, the dust assemblage seems homogeneous and exhibits limited variability over the LGM period, except for the period between 19-20.5 kyr BP (Fig. 1). During this 1.5 kyr interval, Australia and to a lesser extent SAF and PAP contributions peaked while contributions from Patagonia and NZ decreased sharply.

3.2. Heinrich Stadial 1 (Antarctic Isotope Maximum 1) - HS1 (18-14.7 kyr BP)

The HS1 interval marks a rise in $\delta^{18}O$ that is concomitant with a drastic fall of total dust fluxes (Fig. 2B). Despite this drop, the composition of the dust assemblage remained relatively stable along the HS1 when compared to the LGM, with an HS1 average provenance of: PAT ~68%, AUS ~15%, SAF ~8%, NZ 5% and PAP 4% with an average of ~98 different DS combined to fit the dust REE patterns (Fig S7). From ~15.2 kyr BP onwards, PAT contributions fell repeatedly below 50% for the first time since 20.5-19 kyr BP period while SAF and AUS contributions were rising significantly.

3.3. Antarctic Cold Reversal - ACR (14.7 - 12.9 kyr)

The HS1-ACR transition is a turning point in terms of dust composition. SAF and AUS contributions increased greatly (up to 74% and 91%, respectively at 13.671 kyr BP and 13.729 kyr BP) while the contributions of NZ and PAT dropped at their minimum level (i.e., 22 out of 43 samples are <50% of total dust for PAT). As such, the ACR dust is composed of, on average, ~50% PAT, 23% SAF, 21% AUS, 4% PAP and ~3% of dust from NZ with ~72 DS (Fig. S7) combined to fit the dust REE patterns from EDML. In contrast to LGM and HS1 where dust assemblage was relatively homogeneous over time, the provenance of ACR dust (and so as the rest of the ice core) is much more variable (Fig. 1).

3.4. Younger Dryas (YD, 12.9 - 11.7 kyr)

The dust assemblage of YD consists of dust from PAT 44%, SAF 23%, 19% AUS, 8% PAP and 7% NZ with 56 DS involved in the dust mixture on average. Patagonian contributions declined continuously over YD with the 7 steps-mobile average contribution at a minimum (~25% at ~11.5-11.7 kyr BP) corresponding to average flux of 37 µg m^{-2} yr^{-1}. After 14.5 kyr BP up (until ~11 kyr BP), SAF and AUS contributions are comparable, on average ~19-23% (~30 µg m^{-2} yr^{-1}) however their evolutions seem anti-phased to one another.

3.5. Early Holocene (11.7 to 7.5 kyr)

The period is characterized by the lowest total dust flux and large variability over short-timescale in those PSA contributions. The average dust assemblage of the Holocene has 50% PAT, 22% SAF, 13% AUS, 10% PAP and 5% NZ with an average number of 57 DS involved in the Holocene dust assemblage (Fig. S7). Patagonian contributions tend to increase till ~10 kyr BP, drop abruptly between 9.6-9.8 kyr BP and increase again at 9.5 kyr BP (~70% contribution on average) before declining to ~45% at 7.5 kyr BP. The early Holocene is clearly the period of the LGIT where PAP is the most active with contributions up to 71% at 7.951 kyr BP (Fig. 1).

3.6. Comparison between REE and isotopic for dust provenance

In Fig. 3, we compiled the most recent Nd and Sr dataset from the different PSA (grain size < 5μm) across the Southern Hemisphere in order to validate our REE model. Combining the % contributions of each PSA determined by our approach with the average Sr or Nd concentration and isotopic composition values for each of the 6 main PSAs, we calculated the Nd-Sr isotopic ratios for the EDML dust throughout the LGIT (Fig. 3). The idea is to compare those calculated isotopic signatures with the isotopic signatures measured in the E. Antarctic ice cores. Direct isotope measurements for EDML dust are not available, nonetheless our calculated Nd-Sr signatures for EDML dust match well with those of other coring sites in E. Antarctic dust (i.e., EDC, Dome B, Komsomolskaya, old Dome C and Vostok) both for the LGM and the LGIT (Fig. 3). Our calculated isotopic values reproduce well the shift in Nd-Sr signatures observed between LGM and Holocene dust in East Antarctica. This isotopic shift reflects a drop in PAT contributions at the HS1-ACR transition (insert Fig. 3), which is concomitant with an increase of SAF and AUS contributions inducing lower εNd values and more radiogenic $^{87}Sr/^{86}Sr$. The agreement between our calculated Nd-Sr isotopic signatures for EDML and those measured in dust from other sites across E. Antarctica indicates that our model can disentangle the dust PSA contributions throughout the LGIT.

4. Discussion

We have developed a novel statistical model based on the fitting of the REE pattern of dust in ice core using a combination of 207 different REE patterns from well-known PSA across the SH. Applying this method to the REE dataset collected in the EDML ice core, we provide the first, continuous and quantitative record of dust provenance in Antarctica over the LGIT at a decadal to centennial resolution (Figs. 1 and 2). Our provenance record shows that the LGM dust was largely made of Patagonian materials complemented by S-E AUS, SAF and NZ dust (in decreasing order of importance). This dust composition remained roughly stable throughout HS1 despite a massive drop in total deposition, likely caused by an intensification of the 'rainout process' during long-range transport. At ~14.5 kyr BP, the composition of EDML dust abruptly changed with sharp increase in SAF and AUS contributions at the expense of Patagonia. In what follows, we present evidences showing that our dust provenance record is not only in agreement with the existing literature on the dust provenance in E. Antarctica but that it is also coherent with the regional and hemispheric climate evolution of the last interglacial transition.

4.1. LGM (>18 kyr BP): prevalence of high-latitude dust sources (PAT and NZ)

The prevalence of Patagonian dust in EDML during LGM was expected considering that PAT is the closest landmass to E. Antarctica and that EDML is directly downwind to Southern South America sources (Basile et al., 1997; Gaiero, 2007; Gili et al., 2017). Our reconstruction of PAT flux is consistent with those inferred from sediment cores in Laguna Potrok Aike in Southern Patagonia (Haberzettl et al., 2009) and from the Scotia Sea (Weber et al., 2012), that is midway between PAT and EDML (Fig. 4). Sediments from Scotia Sea are of terrigenous origin and exhibit a homogeneous REE patterns, very similar to Patagonian dust (Gaiero et al., 2013). According to our results, the PAT contribution during LGM comes - in large part - from a volcanic/basaltic source. Those observations are coherent with the presence of an extensive Patagonian Ice Sheet covering most of the Andes (2090 km long and 350 km in width at its maximum at 29.4-34 kyr BP - Davies et al., 2020). NZ also developed an ice sheet in the South Island as early as ~33.4 kyr BP (Williams et al., 2015). Up until the onset of deglaciation (Moreno et al., 2015; García et al., 2019; Davies et al., 2020), those ice sheet fed extensive outwash plains on their eastern flanks with high loads of glacial sediment, rich in fine-grained particles. Outwash plains are well-known sources of dust due the constant lateral migration of braided river channels that expose unconsolidated sediments to aeolian deflation (Sugden et al., 2009; Bullard et al., 2016). The eastern outwash plains in PAT and NZ represented also a much larger surface than present-day as sea level was ~135 m below present-day level (Lambeck et al., 2014). Combining sea level change throughout the LGIT with the detailed bathymetry of the Patagonian shelf (Tozer et al., 2019), we calculated that the enlarged continental surface represented an extra 763.10^3 km^2 compared to present-day PAT (~1060.10^3 km^2) and 62.10^3 km^2 for NZ (~150.10^3 km^2) (Figs. 8 and S7 for maps). This shelf expansion probably accentuated the arid nature of the climate on the eastern side of the Andes and in the South Alps and permitted the development of a large networks of braided rivers that spread glacial sediments (Bullard et al., 2016; Sugden et al., 2009). The role of the PAT shelf as a dust supplier to Antarctica during LGM has been discussed previously (e.g., Basile et al., 1997; Gaiero et al., 2003; Gaiero, 2007). While early works presented paleontological evidences (Burckle et al., 1988; Ram et al., 1988), more recent studies provided mineralogical indications pointing towards major contributions from the PAT shelf to E. Antarctica during LGM (Delmonte et al., 2017). The implication of the PAT shelf source is also supported by the persistent presence of leaf wax-derived n-alkanes (C_{25} to C_{35}) in the sedimentary record of the Southern Ocean which suggests a low-altitude source area rather than a higher altitude source glacial/periglacial source (Maher et al., 2010). In terms of geochemistry, the Argentinian shelf shows an isotopic signature (i.e., $-2 < \varepsilon Nd < -4$ and $0.7052 < {}^{87}Sr/{}^{86}Sr < 0.7073$ - (Basile et al., 1997)) and REE patterns that cannot be distinguished from sedimentary and volcanic materials of the PAT continental surface (Gaiero et al., 2003; Gaiero et al., 2004; de Mahiques et al., 2008). That is, the contributions of those emerged shelves are most likely accounted for the contributions of adjacent continents (*i.e*., PAT, NZ) and we considered the Argentinean shelf as being part of the overall PAT dust signature.

Despite the glacial conditions, pollen-inferred vegetation changes indicate millennial-scale reversions from glacial to cold/temperate conditions during the LGM (Figs. 4 and 5). Stratotype of NZ climate documents either two interstadials between 25.6-24.5 kyr BP and 22.6-21.7 kyr BP (Barrell et al., 2013 and references therein) or a single, longer episode of cold/temperate conditions between ~25-23 kyr BP (Augustinus et al., 2011). As for PAT, the only sites east of the Andes providing pollen records of the LGM are posterior to 17 kyr BP (Markgraf et al., 2002). Older pollen records only exist west of the

Andes (i.e., Isla Grande de Chiloé in Fig. 4A; Moreno et al., 2015). Although caution is required to extrapolate those pollen records east of the Andes, Markgraf et al., (2002) showed similar climate trends on both sides of the Andes. As such, episodes of milder climate are described (evidenced by the lowering of *Poaceae* pollen and an increase of arboreal pollen (Moreno et al., 2015) between 23.4-22.6 kyr BP and later 22-19.3 kyr BP that coincide with two periods of low dust flux from PAT and NZ (Figs. 4 and 5) and less complex dust assemblages (Fig. S5A). Those two dust events are unlikely to be related to changes in intensity or in latitude of Southern Westerly Wind (SWW) as pollen records from northwestern PAT and lake-level reconstructions in Lake Cardiel (48.9°S, 71.3°W) have shown a strong and permanent influence of SWW up until 17.5 kyr BP (Moreno et al., 2015; Moreno et al., 2018; Quade and Kaplan, 2017). In our view, the two periods of low dust fluxes - between 22.7-23.7 kyr BP and 19.3-20.5 kyr BP in the PAT (and NZ) records are distinct (Fig. 1). The oldest event is not related to a specific decline of contributions from PAT (i.e., dust assemblage remains unchanged during the interval, Fig. 1) but rather to a drop in total atmospheric deposition in EDML (Fig. 2B) caused by a short-lived episode of milder climate between 23-23.7 kyr BP evidenced by a slight increase of $\delta^{18}O$ in EDML core (Fig. 2B) and a warming of sea surface temperature (Fig. 4E). The lifetime of dust in the atmosphere is constrained by wet deposition (and thus by the water content and temperature - (Lambert et al., 2008; Markle et al., 2018). The milder climate between ~22.7-23.7 kyr BP may thus have reduced the efficiency of long-range dust transport to E. Antarctica without changing the dust assemblage composition, yet this warmer period was short-lived and did not affect the extent of ice-sheet and glacier lobes supplying glaciogenic sediment. In contrast, the 19.3-20.5 kyr BP event of low dust emission comes within a longer interval of milder climate starting ~22 kyr BP in PAT (Fig. 4A) and is characterized by a large shift in dust provenance - i.e., the PAT and NZ contributions dropped while those of SAF and AUS increased (Fig. 1) - without large changes in total atmospheric deposition (Fig. 2B). This drop in PAT contributions is corroborated by a decline in dust flux between 19-20 kyr BP in the Laguna Potrok Aike magnetic susceptibility record (Fig. 4C) and by a warming of the Southern Ocean of ~2°C at ~19.5-22 kyr BP (Fig 4E, (Barker et al., 2009; García et al., 2019; Lamy et al., 2004) leading to the first Antarctic Ice Discharge (AID8 - Fig 8B). Concomitant to this event, there is substantial evidence that ice retreat was underway before 19 kyr BP on a range of Patagonian glaciers

(Markgraf et al., 2007; García et al., 2019; Henríquez et al., 2017). As a result, proglacial (paleo)lakes formed such as the Lago CP (Henríquez et al., 2017) or expanded greatly e.g., Lake Epuyen (42°S), Lake Cholia (42.5°S), Lakes Cisnes-Nirehuao (45°S), Lake Frio (45.7°S) and lakes Balmaceda, Tehuelche and Magellan ((García et al., 2019); (Davies et al., 2020) and references therein). According to Davies *et al.,* (2020)(Davies et al., 2020), the surface of proglacial lakes in Patagonia doubled between 25 kyr BP and 20 kyr BP. Those proglacial lakes might have efficiently trapped glaciogenic sediment, and stalled dust emission from PAT (Sugden et al., 2009). The early onset of deglaciation starting ~22 kyr BP culminating between 20.5-19.3 kyr BP affected primarily the high-latitude PSA. The sudden return of colder conditions between 18-19 kyr BP (Fig 4A, (Barker et al., 2009), (Lamy et al., 2004)) marked the last glacial readvance before the LGM termination documented in large glaciers/lobes in PAT (Bendle et al., 2017; Davies et al., 2020; Kaplan et al., 2008) - but also in south-NZ (Denton et al., 2021). Those glacial readvances, coupled with cooler temperature likely reinitiated the generation of dust from the outwash in high-latitude PSA and the efficient long-range transport to EDML as evidenced in our reconstructions (Fig. 1 and 2) and in Potrok Aike Lake record (Fig. 4C).

4.2 LGM: low-latitude PSA as auxiliary sources of dust (SAF, AUS, PAP)

Dust emission from low latitude PSAs correlate with aridity events and the resulting drying of riverbeds, alluvial fans and large lake systems. According to our results, major low-latitude PSA include, in decreasing order of importance: the Murray and Darling Basins in southeast AUS, the Makgadikgadi complex in Botswana, the Etosha pan and ephemeral coastal rivers in Namibia in SAF and the Puna-Altiplano Plateau (PAP). Climate during LGM over most of southern-west Africa was generally wetter than today with 4-6°C and 8-10°C cooler temperatures in summer and in winter than present-day, respectively (Engelbrecht et al., 2019; Chase and Meadows, 2007). As a result of a northward migration of SWW, an equatorward expansion of the winter rainfall zone was modeled during LGM, with southern Namibia and Botswana being wetter than today, while the present-day summer rainfall regions (south of 22°S) are also projected to have received more rainfall in winter during the LGM (Engelbrecht et al., 2019). This allowed for a northern expansion of the vegetation cover (Lim et al., 2016), resulting in better stabilization of regolith/soils. At first glance, those conditions should have induced a limitation of aeolian deflation and thus lower contributions of SAF dust. Yet, our record shows that SAF experienced two millennial-scale periods of high dust emission between 26.5-25 kyr BP and between 19.3-20.5 kyr BP (Figs. 2 and 6E). We pinpoint the dust of those high-emission periods to originate mostly from the Makgadikgadi lake complex and Etosha pans. Interestingly, the catchments of those two closed-basins are situated in tropical latitudes, i.e., from the Angolan highlands (~12°S) to the southern margins for the Makgadikgadi depression at 24°S and from 15°S to 19°S for the Etosha pan. This means that those basins were mostly unaffected by the increased rainfall brought by the northward shift/expansion of SWW during the LGM. The chronology of lake occupancy in Makgadikgadi complex indicates dry phases at ~23 and ~20 kyr BP (Burrough et al., 2009), also reported in paleo-lake Tsodilo near the Okavango delta between 19-22 kyr BP (Thomas et al., 2003) which corresponds well with millennial-scale aridity phases in Southern Namib desert (Lim et al., 2016) (Fig 6B and 6F). In the Etosha pan, lake level record reveals an intermittent lake with several millennial-scale periods of low level - possibly dry - between 13-28 kyr (Hipondoka et al., 2014). We believe those arid conditions together with dry phases of the Makgadikgadi and Etosha pans were the triggers of an important influx of SAF dust to SH and EDML between 19-20.5 kyr BP (Fig. 6). This assertion is supported by winds intensity proxies and pollen influx measured in sediment cores on Namibian shelf (~26°S and 23°S respectively) and is also in agreement with distal dust flux reported in the Mfabeni Peatland (28°S, N-E of South Africa) both showing respective maxima between 19-21 kyr BP (Figs. 6A, C and D - Humphries et al., 2017).

As for AUS dust (Fig. 7), its record also shows a very noticeable peak between 19-21 kyr BP and a secondary peak between 25-27 kyr BP. Our provenance results pinpoint that most of LGM dust from AUS originated from Darling Basin which experienced an arid climate between 28-18 kyr BP (Builth et al., 2008; Petherick et al., 2008). In Lake Surprise, which is located downwind from Darling Basin in SE-Australia, this aridity is reflected by low value of $\delta^{13}C_{organic\ matter}$ (Fig. 7A) throughout LGM and particularly between 18.5 and 21 kyr BP, concomitant with an increased flux of aeolian deposition (Fig. 7B; Falster et al., 2018). Interestingly, the period of increased effective moisture centered ~24.8 kyr BP in Lake Surprise, which corresponds to a climate amelioration for both NZ (Fig. 5) and AUS (Petherick et al., 2008) and with a warming event in the Southern Ocean to the south of Australia (Calvo et al.,

2007) is also marked by a period of lower dust flux from AUS to EDML (Fig. 7C). Overall, dust records from Lake Surprise and those from other locations from south-eastern and eastern AUS (Fig. 7B, De Deckker et al., 2012); Petherick et al., 2009) match well with our record of AUS contributions and flux in EDML.

The Puna - Altiplano Plateau (PAP) is distinct from the other low latitude PSA as it is located at high altitude (~3600-3800 m.a.s.l.) and bounded by the Western and Eastern cordilleras. PAP is also characterized by several large, interconnected endorheic basins fed by rainfall and thus sensitive to climate transitions. Proxy data from the Central Andes during the LGM suggest cold conditions with an estimated decrease in temperature of 5-8°C (Colinvaux et al., 2000) and dry conditions up until ~25 kyr BP, followed by a slight increase in rainfall (Fornace et al., 2014) allowing for the formation of large paleolakes between ~25 and ~20 kyr BP covering ~21 000 km^2 the so-called 'Sajsi lake' ((Blard et al., 2011); (Placzek et al., 2006)). Our LGM record (Fig. 4F) for PAP dust seems to be directly correlated with the absence/low-stand of paleolakes. Indeed, large fluxes of PAP dust are observed between ~26.5 and 25 kyr BP that correspond to a dry period, followed by a period of minimum dust flux during the 'Sajsi lake cycle' and finally a noticeable emission peak between 20-18 kyr BP when the Sajsi lake regressed (Fig. 4F). Thus, we argue that dust emission from PAP to E. Antarctica is essentially controlled by aridity events at millennial-scale in the central Andes.

4.3 Heinrich Stadial 1 (HS1, 18 - 14.7 kyr BP): warming and stalling of dust flux to E. Antarctica

The warming during HS1 is documented across the SH between ~19 to 17.5 kyr BP by multiple lines of evidence: (*i*) the continuous increase in δ^{18}O values at EDML (Fig. 2B), (*ii*) the warming in the south Atlantic (Fig. 4E) and in the southeast Pacific (Lamy et al., 2004) (*iii*) the rise in temperature of ~8°C in South Patagonia (Pendall et al., 2001). Yet, this increase in temperature in Patagonia was not accompanied by a change in effective precipitation that remained markedly lower than today, following deglaciation (Markgraf et al., 2007; Quade and Kaplan, 2017). Even though the arboreal vegetation expanded largely between ~18.6-17.8 kyr BP on the west side of the Andes (Fig. 4A - (Moreno et al., 2015)), it only spreads eastward through the Andes much later, i.e., between 16-14 kyr BP and was restricted to the piedmont of the Andes (Markgraf et al., 2007; Villa-Martínez and Moreno, 2021). The vegetation of eastern Patagonia remained largely unchanged during HS1 with respect to LGM i.e., dominated by steppe taxa and *Poaceae* (Markgraf et al., 2007). Conversely, the record of Lago Cardiel (48°S - PAT) water level during the HS1 also denotes dry conditions in Patagonia (Quade and Kaplan, 2017). Thus, changes in vegetation type and/or moisture can hardly be invoked to explain the fall of dust emission flux from PAT observed during HS1 (Fig 4B). Nonetheless, the HS1 warming triggered a rapid deglaciation between 18-16.5 kyr BP along the Andes, (García et al., 2019; Davies et al., 2020) and in South-NZ after ~18-17.5 kyr BP (Barrell et al., 2019; Shulmeister et al., 2018) causing an enlargement of proglacial lakes in NZ (Sutherland et al., 2019) and a doubling of glacial lake area in PAT between 20 kyr BP and 15 kyr BP - (Davies et al., 2020 ;Thorndycraft et al., 2019). As discussed above, proglacial lakes potentially affect dust emission solely in high latitude PSAs - PAT and NZ. Yet, here we observe a drastic fall in total dust deposition at EDML after 17.5 kyr BP (Fig. 2B) affecting all PSAs indiscriminately. Indeed, the composition of the HS1 dust remains roughly stable compared to LGM up until ~15 kyr BP (Fig 1). The most logical explanation for this stability in the dust composition is that the lifetime of airborne particles was shorter in the wetter/warmer atmosphere of the HS1 because of a stronger "rainout process" centered in the mid-latitudes acting as a barrier preventing dust to reach the polar regions (Markle et al., 2018). Dust deposits across the Southern Hemisphere tend to support this view showing abrupt decreases in the deposition (in Potrok Aike bog - Fig. 4C; in Scotia Sea - Fig. 4D; in the Namibia continental shelf - Fig. 6A and 6D). This wet period is also evidenced by high-stands between 18-15 kyr BP in the Makgadikgadi complex (Fig. 6F - (Burrough et al., 2009)). A similar declining trend can be observed in AUS dust deposits between 18 and 15 kyr BP (Figs. 7B and 7C) which can be related to wetter conditions (Fig. 7A) in S-E Australia after ~18 kyr BP (Falster et al., 2018; Builth et al., 2008). Our provenance record during HS1 supports the idea that the scavenging of dust by the condensation of water from the atmosphere is a first-order control of the variability of dust deposition in Antarctic ice cores at the millennial timescales.

4.4. Antarctic Cold Reversal (14.7-12.9 kyr BP - ACR): Shift in dust provenance induced by sea level rise and hydrological rearrangement in Patagonia?

The ACR is a millennial-scale cooling event expressed in broad regions of the Southern Ocean, the South Atlantic and land sectors south of 40°S (Pedro et al., 2016). During this interval, SWW shifted southward compared to LGM and were centered ~49°S spanning from 41°S to 58°S in PAT (Quade and Kaplan, 2017). Some glacier advances or stabilization were also documented in Patagonia (McCulloch et al., 2000; Moreno et al., 2009; García et al., 2012; Davies et al., 2020). In terms of vegetation, between 14 and 13 kyr BP, records document a replacement of steppe vegetation by *Nothofagus* woodland in the eastern piedmont of the Andes (Markgraf et al., 2007), however, most of the Patagonian lowlands were still dominated by steppe vegetation with pollen records showing continued aridity throughout the period (Markgraf et al., 2003; Markgraf et al., 2007; Mancini et al., 2013). Lago Cardiel was at its lowest level by 13 kyr BP denoting of very arid conditions at 49°S in PAT (Quade and Kaplan, 2017). All those elements should have played favorably in terms of dust emission from PAT, yet the HS1-ACR transition is marked by a major change in provenance where EDML dust contains less material from PAT and more from lower-latitude PSA (Fig. 1).

Interestingly, the shift at ~14.5 kyr BP (Fig. 1) is not in phase with the massive drop in dust flux ~18 kyr BP (Fig. 2). However, it is coeval with the largest Antarctic Iceberg Discharge (AID6 - Fig. 8B), the onset of the Bølling interstadial in the Northern Hemisphere (14.6 kyr BP) and with a rapid sea-level rise referred to as Meltwater Pulse (MWP1A) occurring 14.65–14.3 kyr BP ((Weber et al., 2014) - Fig. 8C). This transgression submerged a large proportion of the surface that PAT gained during the glacial low-stand (as discussed in section 4.2) and we argue here that it played a major role in the shift of dust composition observed in EDML during the ACR (as well as in EDC ice core – (Gabrielli et al., 2010)). Combining the sea level change over the LGIT (Lambeck et al., 2014) and the bathymetry of NZ and PAT shelves, we inferred the evolution of emerged shelves throughout the LGIT (Fig 8C and S5 for maps). From ~25 to ~16 kyr BP, the NZ and PAT emerged shelves were close to their LGM maximum extension. Crucially, this low stand interval corresponds with the period where the contributions of the high-latitude PSA to EDML were the largest and where the dust assemblage was the most complex but also very much uniform in its composition (Fig. S7A). Between 14.5-14.0 kyr BP, the sea level raised rapidly inducing a fast-paced submersion possibly reaching ~385 km^2 yr^{-1} in PAT (Lambeck et al., 2014). By ~12.9 kyr BP, the sea level reached -70 m and the PAT shelf had shrunk by 70% from to its maximum glacial expansion, with most of the PAT shelf south of 40°S submerged (Fig. S7). We argue that this ACR transgression reduced the area available for aeolian deflation in PAT limiting the contributions of PAT dust to EDML ~14.5 kyr BP. It is important here to note that dust record in the Falklands islands (Monteath et al., 2022) – directly downwind to PAT – also shows a drop in dust flux between 15.5 – 14 kyr BP.

Yet, another 'delayed' consequence of the HS1 warming may have contributed to the abrupt decline of PAT contributions to EDML. The deglaciation opened new drainage pathways westward of the Andes for Patagonian rivers (Davies et al., 2020 and refs. therein). Atlantic-to-Pacific drainage reversals and the eastward shift in the continental water divide had a clear impact on the sediment supply of the Patagonian outwash plains. For instance, the reconfiguration of the Baker and Pascua river catchments that drain to the Pacific involved the capture of ~41 000 km^2 (i.e., the areas surrounding the Lago Pueyrredon/Cochrane and the Lago General Carrera/Buenos Aires) from the eastward-flowing Deseado river catchment (Thorndycraft et al., 2019). The Deseado river catchment is just one of many river basins in PAT that underwent drainage reversal during the LGIT. Caldenius (1932)(Caldenius, 1932) reported drainage reversals from the Chubut drainage basin in northern Patagonia (41–44 °S) down to the Gallegos basin at 52°S. The loss of drainage area in the high Andes (where most of precipitation and erosion occur) induced (i) a weakening of sediment transport to Patagonian outwash plains (Gaiero et al., 2003) but also (ii) a reduction in water discharge that caused, in turn, a shift from braided to meandering river planform (Skirrow et al., 2021). Both of those processes are detrimental to aeolian deflation (Bullard et al., 2016). For Rio Deseado, drainage reversal has been dated to ~15-14 kyr BP (Thorndycraft et al., 2019) but it occurred later (up to ~11 kyr) for other catchments (Glasser et al., 2016; García et al., 2019). For the Rio Chubut, the waning of braided planform was loosely constrained between 12.3±1.0 and 9.4 ± 0.8 kyr BP (Skirrow et al., 2021). The timing of drainage reversals and the ensuing 'deactivation' of Patagonian rivers as sediment conveyors for eolian deflation suggest a diachronous pattern depending on local to regional scale relief and topography. Overall the conjunction of drainage reversals, shift in river planform and the submersion of PAT and NZ shelves altered durably the flux and also the composition of the dust assemblage reaching EDML. The decline of PAT contributions led to a long-lasting increase of the contributions of low-latitude PSA after 14.5 kyr BP

(Fig. 1) throughout the ACR and YD. The decline of PAT contribution may explain the high-frequency variability of the composition of the dust observed since HS1-ACR transition as low-latitude PSA dust are more prone to rain-out processes during atmospheric transport leading to a more variable composition.

4.5. Younger Dryas (YD - 12.9-11.7 kyr BP)

Compared to ACR, the YD in SH is marked by milder conditions evidenced by rising values of the $\delta^{18}O$ record in EDML (Fig. 2B), glacier retreat (Kaplan et al., 2010) and by paleo-vegetation records indicating the onset of warm interglacial conditions after 11.5 kyr BP (Moreno et al., 2009). Yet, several pollen sequences and lake-level reconstruction (e.g., Lago Cardiel) indicate the persistence of arid conditions in the Patagonian plains with precipitation >200 mm during YD (Gilli et al., 2001; Mancini et al., 2013; Quade and Kaplan, 2017). Our YD record shows a continuous decline in PAT contribution and an increase in SAF contribution (Fig. 1) indicating that the processes responsible for the reduction of dust emission from PAT during ACR (see section 4.3) were probably still active. Those phenomena are further compounded by a concomitant shift/weakening of the SWW core southward from 49°S at ∼13 kyr BP to ~ 58°S by ~11 ka (Quade and Kaplan, 2017). The near absence of NZ dust in EDML (Fig. 1) match well with a Late glacial cooler and wetter episode between 13.6-12.4 kyr BP (NZce-3, (Barrell et al., 2013). Our record also shows an anti-phase between SAF and AUS contributions starting ~15.8 kyr BP up until ~ 11 kyr BP with alternating millennial-scale events of high and low contributions (Fig. 1). Similar 500-year-long fluctuations have been reported in deuterium records - δD, a proxy for paleotemperature - in East Antarctica at a pace of ~ 1.0-1.4 kyr during Holocene (Masson et al., 2000). Some of those contribution peaks for AUS and SAF can be related to increased dust emissivity in those regions. For instance, our record shows a sharp increase in AUS contribution between 14.3-13.7 and 13-12.6 kyr BP which could also be noted in Lake Surprise in S-E AUS (in Fig. 7B, (Falster et al., 2018)) and in sediment core MD03-2611 (only the 13-12.6 kyr BP peak) located south of Australia (De Deckker et al., 2012).

Regarding SAF, while dust records are scarce, very arid periods were reported between 14.4-12.5 kyr BP and 10.9-9.3 kyr BP in marine sediment off Namibia (Shi et al., 1998), which might explain the elevated SAF contributions observed in those intervals in our record (Fig. 1). Similarly, the Makgadikgadi pan complex exhibits evidence of drying out at 12.2-11.9 kyr (Burrough et al., 2009) and more broadly, there is evidence of drier conditions in central Southern Africa between 13 to 10 kyr BP compared to ACR and HS1 (Thomas and Shaw, 2002). At this stage, the cause(s) of this AUS-SAF alternance in dust contribution to Antarctica during the 15.8-11 kyr BP interval observed in our provenance record is unclear and warrant further research.

4.6. Early Holocene (11.7-7.5 kyr): prime period for PAP and SAF contributions

Up until ~9 kyr BP, pollen records and lake level reconstructions in eastern PAT document wetter and warmer conditions with a southward shift (possibly between 52°-63°S - (Anderson et al., 2009)) of the SWW over Patagonia ((Mancini et al., 2013); (Quade and Kaplan, 2017); (Villa-Martínez and Moreno, 2021)). This early Holocene optimum is also expressed across E. Antarctica between 11.5 to 9 kyr BP (Masson et al., 2000). Yet, deuterium excess record at EDML shows that this climatic optimum is interrupted by two cold events at ~11.6-11.5 and 9.8-9.6 kyr BP (Stenni et al., 2010). Interestingly, those two cold episodes are well marked by minima (maxima) in PAT (SAF and PAP) contributions and in total dust deposition (Fig. 1 and 2). Stenni *et al.,* (2010) (Stenni et al., 2010) interpreted the ~11.6-11.5 and 9.8-9.6 kyr BP cold events at EDML as reflecting abrupt changes in the air/moisture source areas reaching EDML - possibly towards higher latitude (as opposed to the midlatitude storm track (Reboita et al., 2019)). This interpretation is consistent with the observed sudden drop in PAT contribution at EDML during those cold events.

Apart from the latter two events, our record shows a rise of PAT contributions culminating at 93% at 10.04 kyr BP (Fig.1), mirrored by an increasing trend of atmospheric dust deposition peaking sharply at 10.167-10.147 kyr BP and 10.514-10.411 kyr BP (Fig. 2). The abrupt nature of those peaks is suggestive of large volcanic eruptions. Six volcanoes had major explosive eruptions in Patagonia (Volcanic Explosivity Index of 5) in relative “quick” succession: Mt Burney (9.45±0.64 kyr BP), Chaiten (9.92±0.13 kyr BP), Llaima (10.12±0.1 kyr BP), Yanteles (10.34±0.18 kyr BP), Corcovado (10.34±0.18 kyr BP), Calbuco (10.39±0.1) (Fontijn et al., 2014). There is no record of non-sea-salt sulfate concentration in EDML for the early Holocene, however the timing of those eruptions match

SO_4 peaks in EDC during the 10-11 kyr BP interval (Kurbatov et al., 2006). As EDML is downwind and closer to PAT than EDC, volcanic ash likely reached EDML, hence contributing to the relatively high atmospheric deposition and the increased PAT contributions. The early Holocene also witnessed a shift in fire regime. As early as 12 kyr BP, charcoal records throughout the mid-and high-latitudes of Patagonia (south of 40°S) register a major increase in fire-episode frequency and in their magnitude (Markgraf et al., 2007; Huber et al., 2004). Fire activity was already greater than present at ~12 kyr BP and increased further and became widespread throughout Southern South America at 9.5 kyr BP (Whitlock et al., 2007). Fires co-emit mineral soil-dust particles (Wagner et al., 2021), but also consume the soil-protecting vegetation and induce the breakdown of larger soil aggregates into finer particles favoring aeolian deflation (Dukes et al., 2018). The interval of high fire frequency ended at different times throughout Patagonia: south of 50°S it lasted until 6 kyr BP ((Huber et al., 2004), at ~45°S the reduction in fire occurred between 7-8 kyr BP (Haberle and Bennett, 2004) while, at mid-latitudes (40-42°S), fires were essentially absent after 10 kyr BP (Whitlock et al., 2007). This increased fire activity and the sustained volcanic activity may explain the elevated contribution from PAT throughout the early Holocene (apart from the two cold events at EDML).

Besides PAT, the 11.7-7.5 kyr BP interval is also a prime period for PAP contributions to EDML (Fig. 4F). As discussed above, PAP dust emission is correlated with aridity phases denoted by the drying-out of lakes in the Altiplano. After the Tauca lake phase (~17.5-14.5 kyr) during which a large paleolake formed, the Coipasa lake transgression occurred before 13.3 kyr BP, culminated by ~12.5 kyr BP and regressed completely before 11.5 kyr BP (Blard et al., 2011; Placzek et al., 2006). The ‘Coipasa’ and ‘Tauca’ high-stands correspond well with periods of low dust emission from PAP (Fig. 1 and 4F). In contrast, after 11.5 kyr BP, as no further transgressive-regressive cycles occurred and conditions on the Altiplano were persistently dry (Condom et al., 2004), our record shows an increase of dust contributions. As such, our observations are in line with those of Gili et al., (2017) and Torre et al., (2022) who highlight the role of the Altiplano as a dust supplier during interglacial periods on top of Patagonia’s contribution.

5. Conclusion

Overall, our dust provenance record in EDML suggests a relationship between eustatic sea level, high-latitude PSA hydrology and the composition of atmospheric deposition in the E. Antarctica during LGIT. As such, this study thus opens a new perspective on the use of deep ice cores (and possibly of other type of dust deposits such as loess, peat or sediment) as archives of dust provenance. Our approach nonetheless has some limitations that could potentially impact the reconstructed provenance record. Our statistical approach is empirically constrained by a REE pattern database covering the major PSA in the SH implying that our result could potentially be modified by the addition of missing sources or more representative samples in each PSA. Our model would also benefit from a better geochemical characterization of Australian dust (that is, its fine fractions) or a larger cover of Southern Africa dust/topsoil (in particular, from paleolakes areas). At the other end of our statistical analysis, the precision of REE patterns in ice cores could be improved by analyzing total REE concentrations - at least in some portions - instead of relying on partial dissolution. To correct for partial dust dissolution of dust, we applied *cf* values which were determined in EDC (on a limited of set of samples) to the EDML REE dataset. Although dust deposition EDC and EDML are close in term of composition, *cf* values would need to be determined in EDML on a representative set of samples to refine further our provenance record. With this study, we hope to encourage future studies to place greater emphasis on the use of REE to trace dust provenance over time.

Acknowledgments and funding

S. Bonneville acknowledges the support of the Fonds National de la Recherche Scientifique (FRS-FNRS CDR-J.0017.22). A. Vanderstraeten was supported at the LOG by the CaPPA project (Chemical and Physical Properties of the Atmosphere) funded by ANR (ANR-ll-LABX-0005-01), and the CNES (TOSCA/DOC project). N. Mattielli acknowledges the BRAIN-be funding for the CHASE Antarctica research program (BR/175/A2/Chase). The CESAM chamber team is acknowledged for their help to obtain fine fraction of SAF samples. This CNRS-INSU facility received funding from the European Union's Horizon 2020 research and innovation program through the EUROCHAMP-2020 Infrastructure Activity (No. 730997). Sample collection was supported by the Natural Science and Engineering Research Council of Canada (Discovery Grant RGPIN-2016-05417). Fieldwork in Namibia was supported through permits issued by the Ministry of the Environment and Transport (#2255/2017) and the National Commission on Research, Science, & Technology (#RPIV00272018). We are grateful to J. King, M. Hipondoka, G.Maggs-Kölling, and the Gobabeb Research and Training Centre for the collection of the field samples.

Data availability

All data needed to evaluate the conclusions in the paper are present in the paper and/or the Supplementary Materials. Additional data related to the paper may be requested from the authors. Correspondence and requests should be addressed to S.B.

Contributions

St.B. directed the research and wrote the manuscript. St.B, A.V. and G.L. developed together the model. Sy.B, A.B. and A.V. performed the size fractionation of Namibian samples and their analysis. A.V. did the isotopic back-calculations. All authors discussed the results and commented on the manuscript.

Competing Interest: The authors declare no competing interests.

668

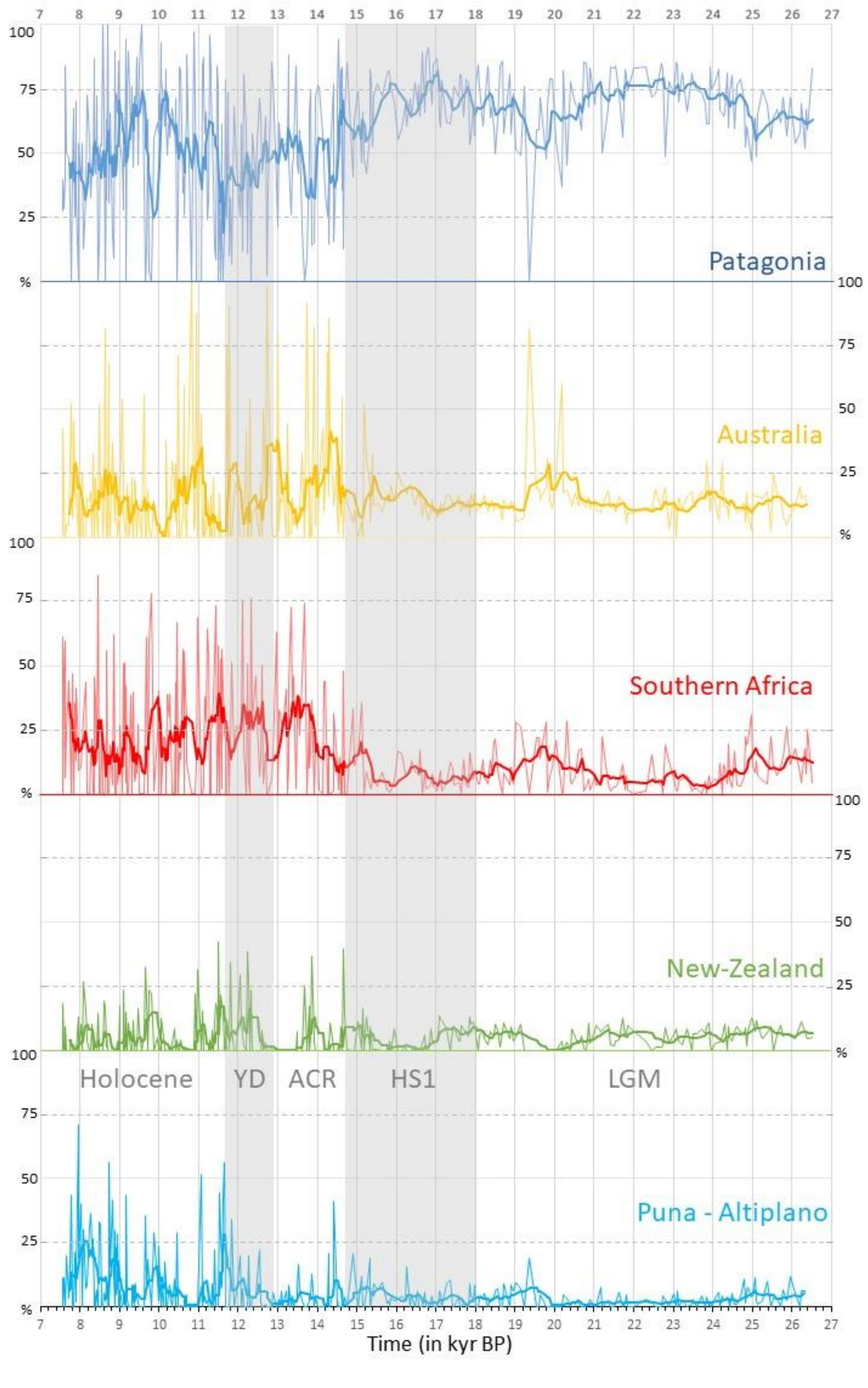
Patagonia
Australia
Southern Africa
New-Zealand
Holocene
YD
ACR
HS1
LGM
Puna - Altiplano
Time (in kyr BP)

Figure 1: Evolution of contributions to EDML from PSA between 7.55 and 26.55 kyr (% of total dust deposition). Bold lines denote the mobile average over 7 steps (~289 years). Gray vertical zones delineate the various epochs of the transition from LGM to Holocene. Central-Western-Argentina is not shown as its contribution is very low, between 0.03 to 0.3 % of the total deposition in EDML. 95% confidence interval for each time-step is plotted in Fig S5 of Supplementary Materials.

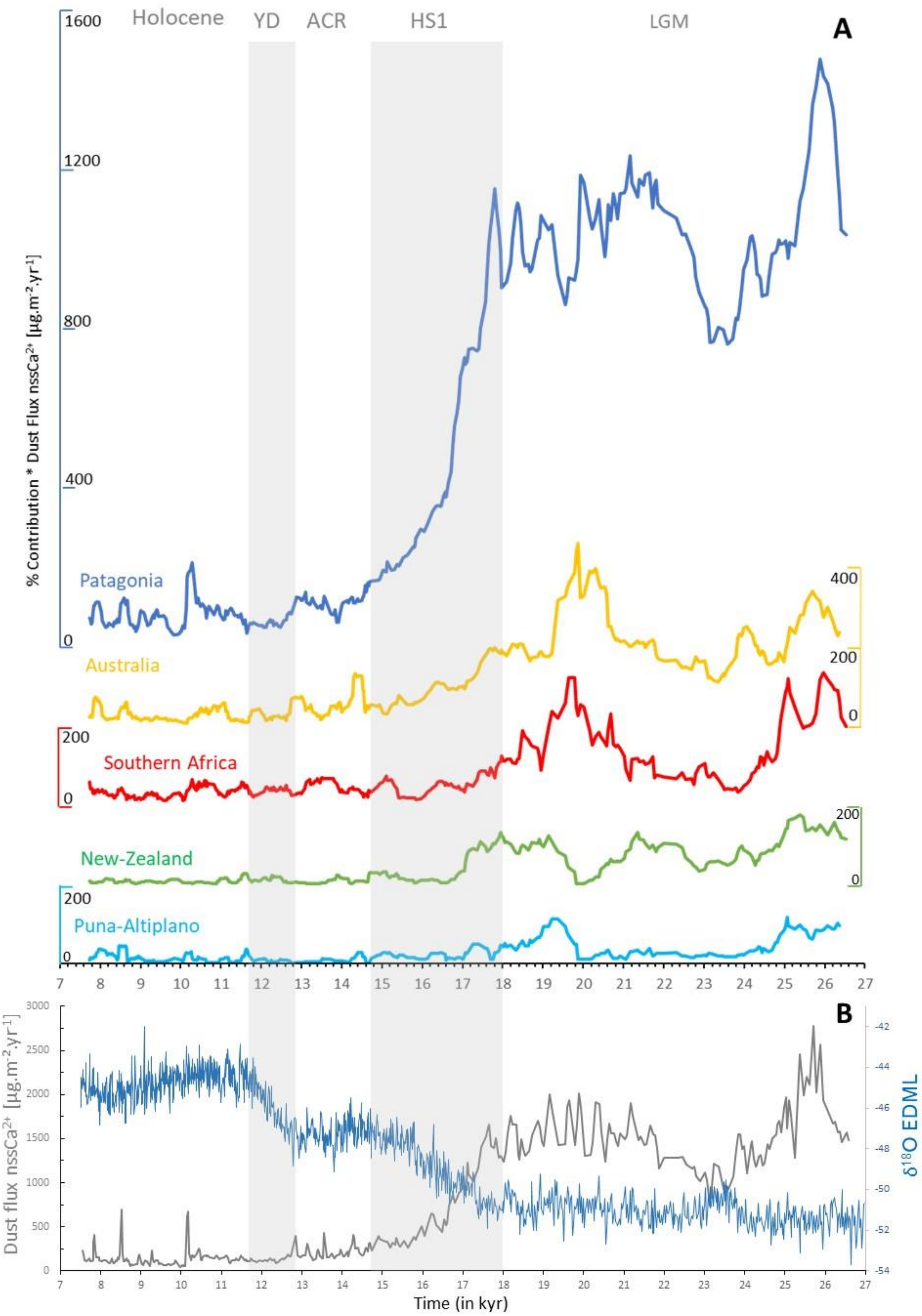

Figure 2 : (A) Reconstruction of fluxes from large PSA to EDML (5-steps mobile average) based on the contribution of large PSA (Fig. 1) and the $nssCa^{2+}$ flux to EDML from (Fischer et al., 2007) shown in (B) together with the record of $\delta^{18}O$ in EDML (Barbante et al., 2006).

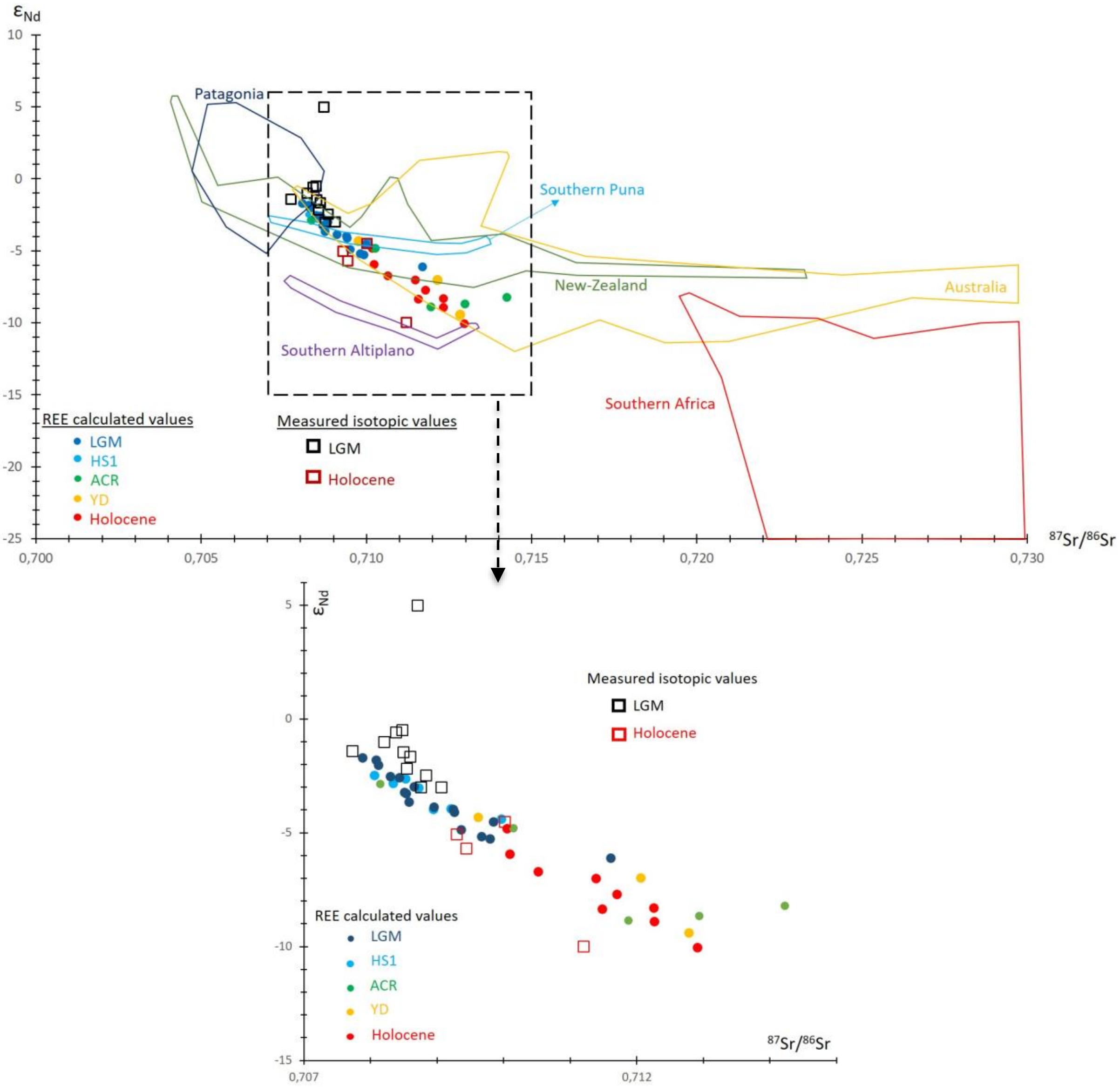

Figure 3 and insert: Compilation of $^{87}Sr/^{86}Sr$ and ε_{Nd} isotopic fingerprint representative of PSA, dust in ice core (red and black squares for Holocene and LGM samples respectively) and calculated isotopic values using REE contributions from EDML (this study - colored dots). Colored-frame areas denote the domains of isotopic values of respective PSA used for the isotope calculation, i.e., involved in the dust assemblage (data from Grousset et al., 1992; Delmonte et al., 2004; Gingele and De Deckker, 2005 ; De Deckker et al., 2014; Revel-Rolland et al., 2006; Gaiero, 2007; Gili et al., 2017 ; Gili et al., 2022; Li et al., 2020; Koffman et al., 2021). Note that the SAF domain has an angular frame at high radiogenic values as ε_{Nd} of -25 are published without the corresponding $^{87}Sr/^{86}Sr$ ratio (Li et al., 2020). Note also that both SAF and AUS domains expands beyond the limit of the graph with dust samples $^{87}Sr/^{86}Sr$ > 0.730 (not shown here). Black squares represent LGM and glacial dust samples from EDC *(stage 2, 4 and 6), Vostok (4 to 12), Dome B, Komsomolskaya and old Dome C (Grousset et al., 1992; Basile et al., 1997 ; Delmonte et al., 2004 ; Delmonte et al., 2010). Red squares correspond to Holocene dust isotopic signature measured in EDC and Vostok dust (Delmonte et al., 2007). REE-based calculated isotopic fingerprints (blue to red dots corresponding to the 5 epochs among LGIT) were obtained from (i) the % contributions of PSA (Table S3 – data shown here are composition averaged over 500-year periods) and (ii) the isotopic fingerprint and elemental concentration of the PSAs end-members (Table S4).*

699 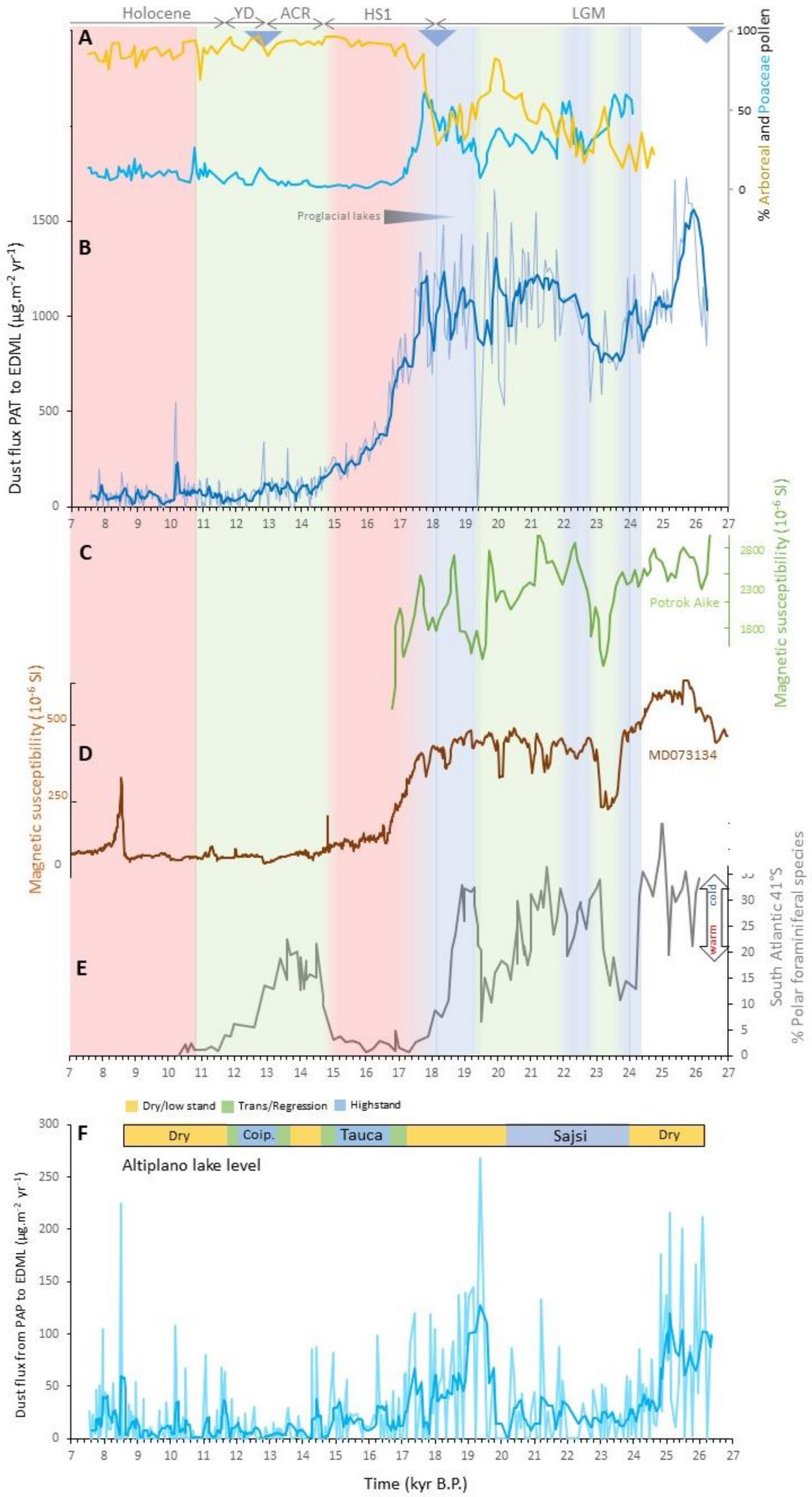
Holocene
YD
ACR
HS1
LGM
A
% Arboreal and Poaceae pollen
Proglacial lakes
B
Dust flux PAT to EDML (µg.m-2 yr-1)
C
Potrok Aike
Magnetic susceptibility (10-6 SI)
D
MD073134
Magnetic susceptibility (10-6 SI)
E
cold
warm
South Atlantic 41°S
% Polar foraminiferal species
Dry/low stand
Trans/Regression
Highstand
F
Dry
Coip.
Tauca
Sajsi
Dry
Altiplano lake level
Dust flux from PAP to EDML (µg.m-2 yr-1)
Time (kyr B.P.)

*Figure 4: (**A**) Light blue and orange lines represent respectively the record of Poaceae (a proxy for dryer conditions) and arboreal pollens (a proxy for wetter, moist climate) from Canal de la Puntilla and Huelmo sites (41-42°S) in Chiloe Island in northwestern Patagonia (data from Moreno et al., 2015). The vertical blue bars represent extreme glacial conditions, green bars represent cold-temperate conditions, red bars represent warm climatic conditions based on changes of pollen-inferred vegetation in (Moreno et al., 2015). (**B**) Reconstruction of dust flux in EDML from Patagonia (dark blue line) between 7.55 and 26.5 kyr. Triangles denotes of major ice advances ~27 kyr, ~18 kyr and 13 kyr in the Southern Andes at 37°S (Davies et al., 2020; García et al., 2019). (**C** and **D**) Magnetic susceptibility records used as a proxy of dust flux from PAT in sites MD07-3134 (in Scotia Sea at 57°26'S 43°27'W) and Potrok Aike lake located in southern PAT at 51°57S 70°22'W (data from Weber et al., (2012) and Haberzettl et al., 2009)-. (**E**) Percentage of polar foraminiferal species in South Atlantic at TNO57-21 site 41°08'S 7°49'E (data from Barker et al., 2009)). (**F**) Evolution of dust flux in EDML from Puna-Altiplano Plateau (PAP) with paleolake level reconstruction from shoreline dating in the southern basin of the Altiplano from (Blard et al., 2011) and (Placzek et al., 2006).*

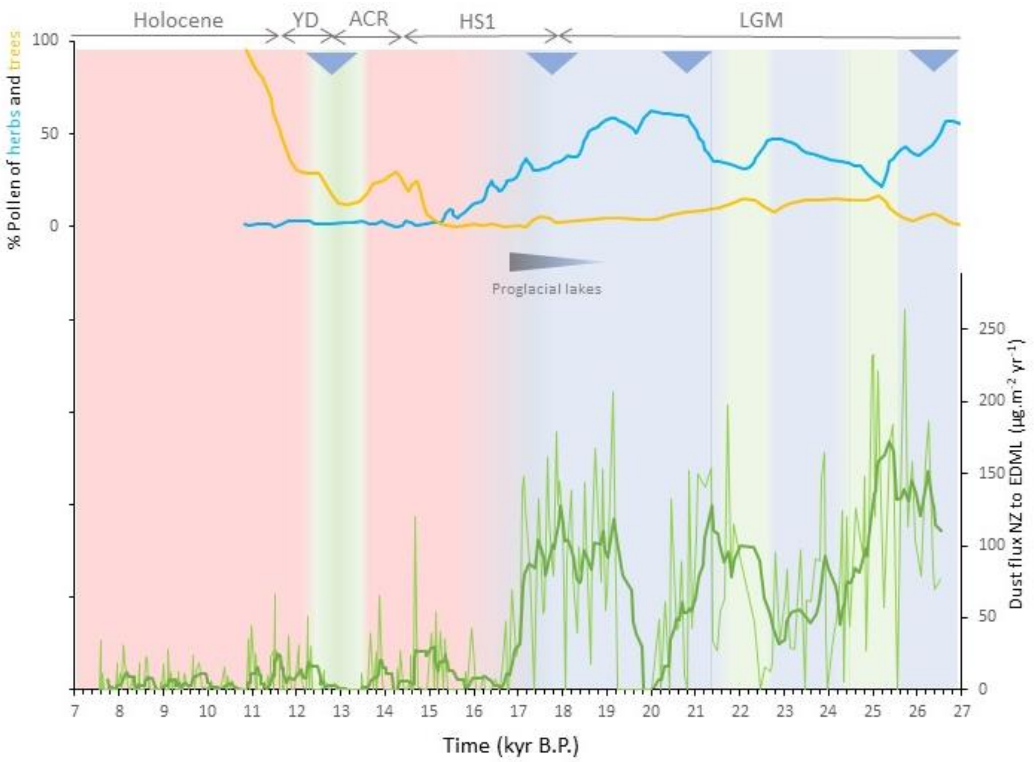

722

723 *Figure 5: (A) Evolution of dust flux in EDML from New Zealand (green line) between 7.55 and 26.5*
724 *kyr. Orange and dark blue lines denote tall forest tree and herbfield pollens from Okarito Lagoon,*
725 *Westland, S-NZ (data from Williams et al., 2015). The vertical blue bars represent extreme glacial*
726 *conditions, green bars represent cold/temperate conditions, red bars represent warm conditions*
727 *according to NZ-INTIMATE climate event stratigraphy (Barrell et al., 2013). Time interval for*
728 *proglacial lake formation in SNZ was compiled from ((Sutherland et al., 2019) while major ice advances*
729 *are reported at ~27 kyr, 23-22 kyr, ~20 kyr, ~18 kyr and later ~13 kyr at the transition ACR/YD. (Denton*
730 *et al., 2021; Kaplan et al., 2010).*

731

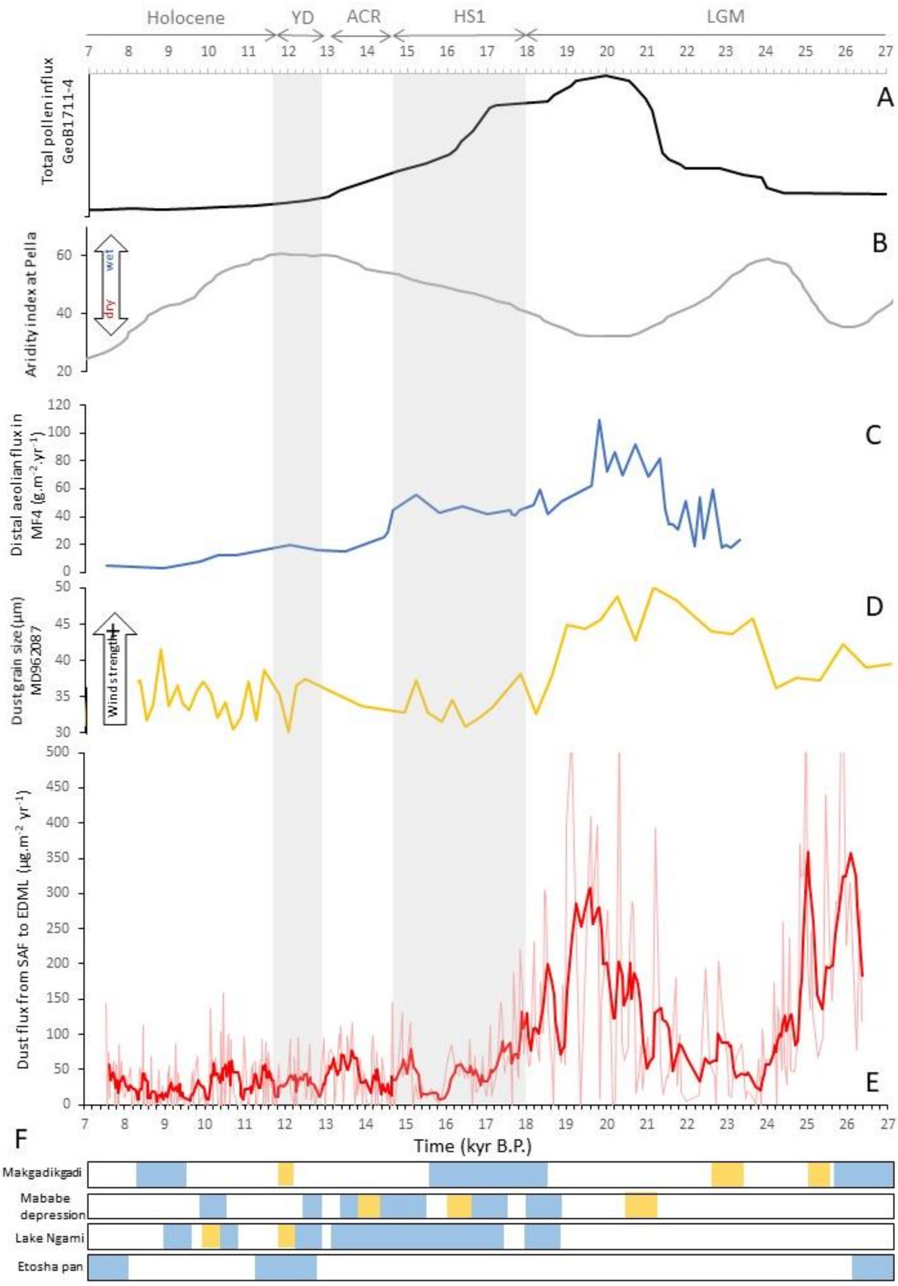

Figure 6 : Evolution of dust flux in EDML from Southern Africa (E) compared with marine and terrestrial proxies of regional climate. (A) Total pollen flux (indicator of trade wind intensity) in site GeoB1711-4 located on Namibia continental slope (data from Shi et al., 2001). (B) Aridity Index based on vegetation pollen records found near Pella, N-W South Africa (data from Lim et al., 2016). (C) Distal aeolian dust flux to Mfabeni Peatland - East coast of Southern Africa (data from (Humphries et al., 2017). (D) Coarse-grained dust diameters (wind strength proxy) recorded in MD962087 core on the Namibian continental slope (25°6'S, 13°38'E) (Pichevin et al., 2005). (E) Highstands (blue bars) in the Makgadikgadi lake, Ngami lake and Mababe depression (i.e., Paleo-megalake Makgadikgadi system)

and Etosha systems. Orange bars refer to periods where there is evidence for very low or absent lakes (Burrough et al., 2009).

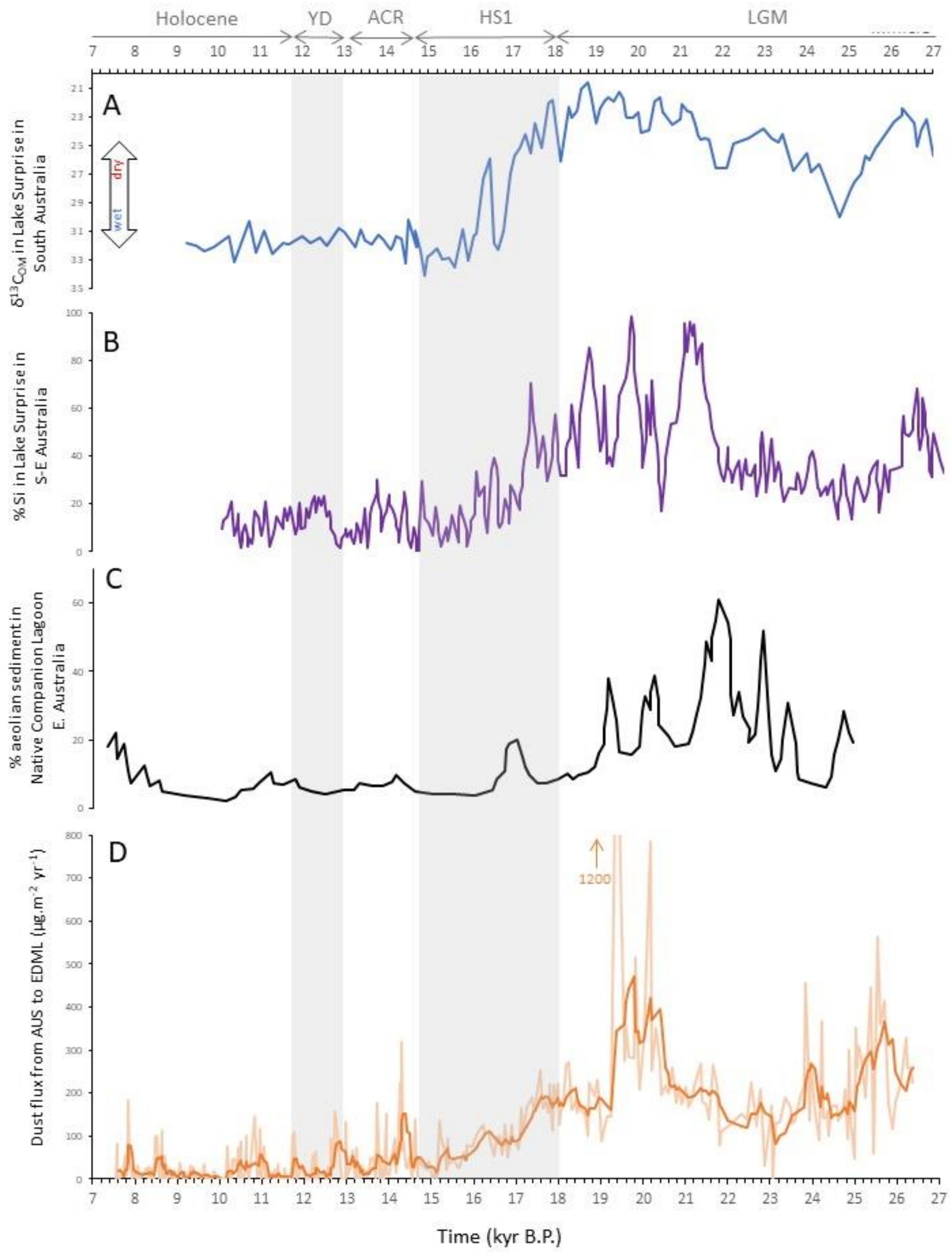

*Figure 7 : (**D**) Evolution of dust flux from AUS to EDML between 7-27 kyr compared to $\delta^{13}C$ of organic matter (**A**) and Si flux (**B**) in Lake Surprise (south-eastern Australia - 38.06°S 141.91°W) respectively (data from (Falster et al., 2018)). (**C**) denote the % of aeolian content in Native Companion Lagoon in Eastern Australia (27°30'S 153°30'E, data from (Petherick et al., 2009)).*

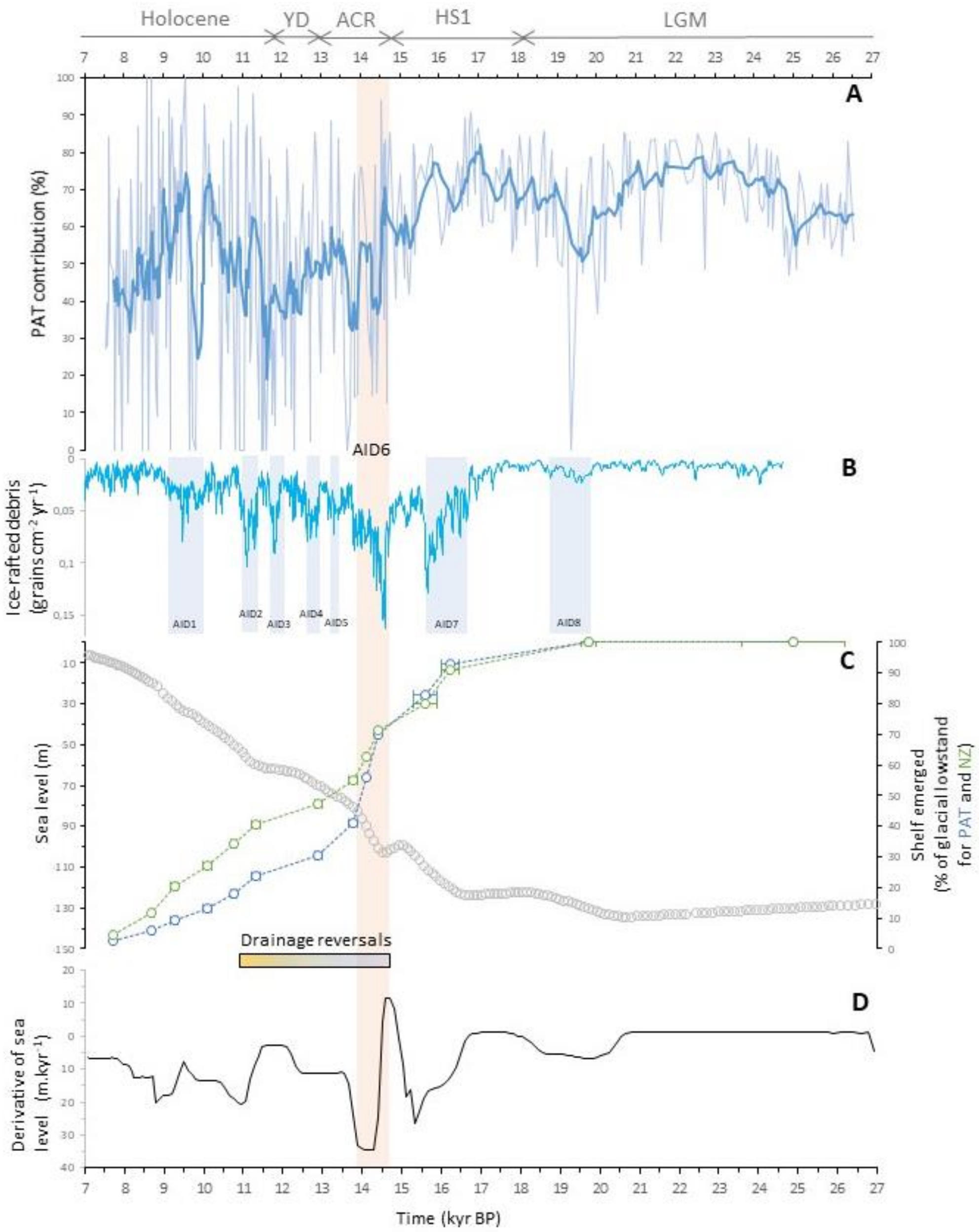

*Figure 8: (**A**) Contributions of PAT to EDML during the last glacial-interglacial transition (% contributions in pale blue line and 7-steps mobile average in bold blue line). (**B**) Record of iceberg-rafted debris flux in Scotia Sea showing eight phases of Antarctic Iceberg Discharge events (AID1 to AID8) at approximately 20–19 kyr ago, 17–16 kyr ago, 15–14 kyr ago, 13.5 kyr ago, 13 kyr ago, 12 kyr ago, 11 kyr ago and 10–9 kyr ago (vertical shading data from* (Weber et al., 2014)*). (**C**) Sea level (in m) between 7-27 kyr BP (open gray symbols - data from* (Lambeck et al., 2014)*) and associated decrease of continental shelf surface area in PAT (open blue symbols) and south-NZ (open green symbols) with respect to maximum glacial low-stand. (**D**) Derivative of sea level between 7-27 kyr BP highlighting a major submersion between 14-15 kyr BP.*

References

Anderson, R.F., Ali, S., Bradtmiller, L.I., Nielsen, S.H.H., Fleisher, M.Q., Anderson, B.E., Burckle, L.H., 2009. Wind-Driven Upwelling in the Southern Ocean and the Deglacial Rise in Atmospheric CO2. Science 323, 1443–1448. https://doi.org/10.1126/science.1167441

Augustinus, P., D’costa, D., Deng, Y., Hagg, J., Shane, P., 2011. A multi-proxy record of changing environments from ca. 30 000 to 9000 cal. a BP: Onepoto maar palaeolake, Auckland, New Zealand. Journal of Quaternary Science 26, 389–401. https://doi.org/10.1002/jqs.1463

Barbante, C., Barnola, J.-M., Becagli, S., Beer, J., Bigler, M., Boutron, C., Blunier, T., Castellano, E., Cattani, O., Chappellaz, J., Dahl-Jensen, D., Debret, M., Delmonte, B., Dick, D., Falourd, S., Faria, S., Federer, U., Fischer, H., Freitag, J., Frenzel, A., Fritzsche, D., Fundel, F., Gabrielli, P., Gaspari, V., Gersonde, R., Graf, W., Grigoriev, D., Hamann, I., Hansson, M., Hoffmann, G., Hutterli, M.A., Huybrechts, P., Isaksson, E., Johnsen, S., Jouzel, J., Kaczmarska, M., Karlin, T., Kaufmann, P., Kipfstuhl, S., Kohno, M., Lambert, F., Lambrecht, Anja, Lambrecht, Astrid, Landais, A., Lawer, G., Leuenberger, M., Littot, G., Loulergue, L., Lüthi, D., Maggi, V., Marino, F., Masson-Delmotte, V., Meyer, H., Miller, H., Mulvaney, R., Narcisi, B., Oerlemans, J., Oerter, H., Parrenin, F., Petit, J.-R., Raisbeck, G., Raynaud, D., Röthlisberger, R., Ruth, U., Rybak, O., Severi, M., Schmitt, J., Schwander, J., Siegenthaler, U., Siggaard-Andersen, M.-L., Spahni, R., Steffensen, J.P., Stenni, B., Stocker, T.F., Tison, J.-L., Traversi, R., Udisti, R., Valero-Delgado, F., van den Broeke, M.R., van de Wal, R.S.W., Wagenbach, D., Wegner, A., Weiler, K., Wilhelms, F., Winther, J.-G., Wolff, E., EPICA Community Members, 2006. One-to-one coupling of glacial climate variability in Greenland and Antarctica. Nature 444, 195–198. https://doi.org/10.1038/nature05301

Barker, S., Diz, P., Vautravers, M.J., Pike, J., Knorr, G., Hall, I.R., Broecker, W.S., 2009. Interhemispheric Atlantic seesaw response during the last deglaciation. Nature 457, 1097–1102. https://doi.org/10.1038/nature07770

Barrell, D.J.A., Almond, P.C., Vandergoes, M.J., Lowe, D.J., Newnham, R.M., 2013. A composite pollen-based stratotype for inter-regional evaluation of climatic events in New Zealand over the past 30,000 years (NZ-INTIMATE project). Quaternary Science Reviews 74, 4–20. https://doi.org/10.1016/j.quascirev.2013.04.002

Barrell, D.J.A., Putnam, A.E., Denton, G.H., 2019. Reconciling the onset of deglaciation in the upper Rangitata valley, Southern Alps, New Zealand. Quaternary Science Reviews 203, 141–150. https://doi.org/10.1016/j.quascirev.2018.11.003

Basile, I., Grousset, F.E., Revel, M., Petit, J.R., Biscaye, P.E., Barkov, N.I., 1997. Patagonian origin of glacial dust deposited in East Antarctica (Vostok and Dome C) during glacial stages 2, 4 and 6. Earth and Planetary Science Letters 146, 573–589. https://doi.org/10.1016/S0012-821X(96)00255-5

Bendle, J.M., Palmer, A.P., Thorndycraft, V.R., Matthews, I.P., 2017. High-resolution chronology for deglaciation of the Patagonian Ice Sheet at Lago Buenos Aires (46.5°S) revealed through varve chronology and Bayesian age modelling. Quaternary Science Reviews 177, 314–339. https://doi.org/10.1016/j.quascirev.2017.10.013

Blard, P.-H., Sylvestre, F., Tripati, A.K., Claude, C., Causse, C., Coudrain, A., Condom, T., Seidel, J.-L., Vimeux, F., Moreau, C., Dumoulin, J.-P., Lavé, J., 2011. Lake highstands on the Altiplano (Tropical Andes) contemporaneous with Heinrich 1 and the Younger Dryas: new insights from 14C, U–Th dating and δ18O of carbonates. Quaternary Science Reviews 30, 3973–3989. https://doi.org/10.1016/j.quascirev.2011.11.001

Bory, A., Wolff, E., Mulvaney, R., Jagoutz, E., Wegner, A., Ruth, U., Elderfield, H., 2010. Multiple sources supply eolian mineral dust to the Atlantic sector of coastal Antarctica: Evidence from recent snow layers at the top of Berkner Island ice sheet. Earth and Planetary Science Letters 291, 138–148. https://doi.org/10.1016/j.epsl.2010.01.006

Builth, H., Kershaw, A.P., White, C., Roach, A., Hartney, L., McKenzie, M., Lewis, T., Jacobsen, G., 2008. Environmental and cultural change on the Mt Eccles lava-flow landscapes of southwest Victoria, Australia. The Holocene 18, 413–424. https://doi.org/10.1177/0959683607087931

Bullard, J.E., Baddock, M., Bradwell, T., Crusius, J., Darlington, E., Gaiero, D., Gassó, S., Gisladottir, G., Hodgkins, R., McCulloch, R., McKenna-Neuman, C., Mockford, T., Stewart, H., Thorsteinsson, T., 2016. High-latitude dust in the Earth system. Reviews of Geophysics 54, 447–485. https://doi.org/10.1002/2016RG000518

Burckle, L.H., Gayley, R.I., Ram, M., Petit, J.-R., 1988. Diatoms in Antarctic ice cores: Some implications for the glacial history of Antarctica. Geology 16, 326–329. https://doi.org/10.1130/0091-7613(1988)016<0326:DIAICS>2.3.CO;2

Burrough, S.L., Thomas, D.S.G., Bailey, R.M., 2009. Mega-Lake in the Kalahari: A Late Pleistocene record of the Palaeolake Makgadikgadi system. Quaternary Science Reviews 28, 1392–1411. https://doi.org/10.1016/j.quascirev.2009.02.007

Caldenius, C.C., 1932. Las Glaciaciones Cuaternarias en la Patagonia y Tierra del Fuego. Geografiska Annaler 14, 1–164. https://doi.org/10.1080/20014422.1932.11880545

Calvo, E., Pelejero, C., De Deckker, P., Logan, G.A., 2007. Antarctic deglacial pattern in a 30 kyr record of sea surface temperature offshore South Australia. Geophysical Research Letters 34. https://doi.org/10.1029/2007GL029937

Chase, B.M., Meadows, M.E., 2007. Late Quaternary dynamics of southern Africa’s winter rainfall zone. Earth-Science Reviews 84, 103–138. https://doi.org/10.1016/j.earscirev.2007.06.002

Colinvaux, P.A., De Oliveira, P.E., Bush, M.B., 2000. Amazonian and neotropical plant communities on glacial time-scales: The failure of the aridity and refuge hypotheses. Quaternary Science Reviews 19, 141–169. https://doi.org/10.1016/S0277-3791(99)00059-1

Condom, T., Coudrain, A., Dezetter, A., Brunstein, D., Delclaux, F., Jean-Emmanuel, S., 2004. Transient modelling of lacustrine regressions: two case studies from the Andean Altiplano. Hydrological Processes 18, 2395–2408. https://doi.org/10.1002/hyp.1470

Coppo, R., Cosentino, N.J., Torre, G., del Rio, I., Sawakuchi, A.O., Berman, A.L., Koester, E., Delmonte, B., Gaiero, D.M., 2022. Coeval minimum south American and maximum Antarctic last glacial maximum dust deposition: A causal link? Quaternary Science Reviews 295, 107768. https://doi.org/10.1016/j.quascirev.2022.107768

Davies, B.J., Darvill, C.M., Lovell, H., Bendle, J.M., Dowdeswell, J.A., Fabel, D., García, J.-L., Geiger, A., Glasser, N.F., Gheorghiu, D.M., Harrison, S., Hein, A.S., Kaplan, M.R., Martin, J.R.V., Mendelova, M., Palmer, A., Pelto, M., Rodés, Á., Sagredo, E.A., Smedley, R.K., Smellie, J.L., Thorndycraft, V.R., 2020. The evolution of the Patagonian Ice Sheet from 35 ka to the present day (PATICE). Earth-Science Reviews 204, 103152. https://doi.org/10.1016/j.earscirev.2020.103152

De Deckker, P., Moros, M., Perner, K., Jansen, E., 2012. Influence of the tropics and southern westerlies on glacial interhemispheric asymmetry. Nature Geoscience 5, 266–269. https://doi.org/10.1038/ngeo1431

De Deckker, P., Munday, C.I., Brocks, J., O'Loingsigh, T., Allison, G.E., Hope, J., Norman, M., Stuut, J.-B.W., Tapper, N.J., van der Kaars, S., 2014. Characterisation of the major dust storm that traversed over eastern Australia in September 2009; a multidisciplinary approach. Aeolian Research 15, 133–149. https://doi.org/10.1016/j.aeolia.2014.07.003

De Deckker, P., Norman, M., Goodwin, I.D., Wain, A., Gingele, F.X., 2010. Lead isotopic evidence for an Australian source of aeolian dust to Antarctica at times over the last 170,000years. Palaeogeography, Palaeoclimatology, Palaeoecology 285, 205–223. https://doi.org/10.1016/j.palaeo.2009.11.013

de Mahiques, M.M., Tassinari, C.C.G., Marcolini, S., Violante, R.A., Figueira, R.C.L., da Silveira, I.C.A., Burone, L., de Mello e Sousa, S.H., 2008. Nd and Pb isotope signatures on the Southeastern South American upper margin: Implications for sediment transport and source rocks. Marine Geology 250, 51–63. https://doi.org/10.1016/j.margeo.2007.11.007

Delmonte, B., Baroni, C., Andersson, P.S., Schoberg, H., Hansson, M., Aciego, S., Petit, J.-R., Albani, S., Mazzola, C., Maggi, V., Frezzotti, M., 2010. Aeolian dust in the Talos Dome ice core (East Antarctica, Pacific/Ross Sea sector): Victoria Land versus remote sources over the last two climate cycles. Journal of Quaternary Science 25, 1327–1337. https://doi.org/10.1002/jqs.1418

Delmonte, B., Basile-Doelsch, I., Petit, J.-R., Maggi, V., Revel-Rolland, M., Michard, A., Jagoutz, E., Grousset, F., 2004. Comparing the Epica and Vostok dust records during the last 220,000 years: stratigraphical correlation and provenance in glacial periods. Earth-Science Reviews 66, 63–87. https://doi.org/10.1016/j.earscirev.2003.10.004

Delmonte, B., Paleari, C.I., Andò, S., Garzanti, E., Andersson, P.S., Petit, J.R., Crosta, X., Narcisi, B., Baroni, C., Salvatore, M.C., Baccolo, G., Maggi, V., 2017. Causes of dust size variability in central East Antarctica (Dome B): Atmospheric transport from expanded South American sources during Marine Isotope Stage 2. Quaternary Science Reviews 168, 55–68. https://doi.org/10.1016/j.quascirev.2017.05.009

Delmonte, B., Robert Petit, J., Basile-Doelsch, I., Jagoutz, E., Maggi, V., 2007. 6. Late quaternary interglacials in East Antarctica from ice-core dust records, in: Sirocko, F., Claussen, M., Sánchez Goñi, M.F., Litt, T. (Eds.), Developments in Quaternary Sciences. Elsevier, pp. 53–73. https://doi.org/10.1016/S1571-0866(07)80031-5

Delmonte, B., Winton, H., Baroni, M., Baccolo, G., Hansson, M., Andersson, P., Baroni, C., Salvatore, M.C., Lanci, L., Maggi, V., 2020. Holocene dust in East Antarctica: Provenance and variability in time and space. The Holocene 30, 546–558. https://doi.org/10.1177/0959683619875188

Denton, G.H., Putnam, A.E., Russell, J.L., Barrell, D.J.A., Schaefer, J.M., Kaplan, M.R., Strand, P.D., 2021. The Zealandia Switch: Ice age climate shifts viewed from Southern Hemisphere moraines. Quaternary Science Reviews 257, 106771. https://doi.org/10.1016/j.quascirev.2020.106771

Diaz, M.A., Welch, S.A., Sheets, J.M., Welch, K.A., Khan, A.L., Adams, B.J., McKnight, D.M., Cary, S.C., Lyons, W.B., 2020. Geochemistry of aeolian material from the McMurdo Dry Valleys, Antarctica: Insights into Southern Hemisphere dust sources. Earth and Planetary Science Letters 547, 116460. https://doi.org/10.1016/j.epsl.2020.116460

Dick, D., Wegner, A., Gabrielli, P., Ruth, U., Barbante, C., Kriews, M., 2008. Rare earth elements determined in Antarctic ice by inductively coupled plasma—Time of flight, quadrupole and sector field-mass spectrometry: An inter-comparison study. Analytica Chimica Acta 621, 140–147. https://doi.org/10.1016/j.aca.2008.05.026

Dukes, D., Gonzales, H.B., Ravi, S., Grandstaff, D.E., Van Pelt, R.S., Li, J., Wang, G., Sankey, J.B., 2018. Quantifying Postfire Aeolian Sediment Transport Using Rare Earth Element Tracers. Journal of Geophysical Research: Biogeosciences 123, 288–299. https://doi.org/10.1002/2017JG004284

Engelbrecht, F.A., Marean, C.W., Cowling, R.M., Engelbrecht, C.J., Neumann, F.H., Scott, L., Nkoana, R., O'Neal, D., Fisher, E., Shook, E., Franklin, J., Thatcher, M., McGregor, J.L., Van der Merwe, J., Dedekind, Z., Difford, M., 2019. Downscaling Last Glacial Maximum climate over southern Africa. Quaternary Science Reviews 226, 105879. https://doi.org/10.1016/j.quascirev.2019.105879

Falster, G., Tyler, J., Grant, K., Tibby, J., Turney, C., Löhr, S., Jacobsen, G., Kershaw, A.P., 2018. Millennial-scale variability in south-east Australian hydroclimate between 30,000 and 10,000 years ago. Quaternary Science Reviews 192, 106–122. https://doi.org/10.1016/j.quascirev.2018.05.031

Fathi Hafshejani, S., Moaberfard, Z., 2022. Initialization for non-negative matrix factorization: a comprehensive review. International Journal of Data Science and Analytics. https://doi.org/10.1007/s41060-022-00370-9

Fischer, H., Fundel, F., Ruth, U., Twarloh, B., Wegner, A., Udisti, R., Becagli, S., Castellano, E., Morganti, A., Severi, M., Wolff, E., Littot, G., Röthlisberger, R., Mulvaney, R., Hutterli, M.A., Kaufmann, P., Federer, U., Lambert, F., Bigler, M., Hansson, M., Jonsell, U., de Angelis, M., Boutron, C., Siggaard-Andersen, M.-L., Steffensen, J.P., Barbante, C., Gaspari, V., Gabrielli, P., Wagenbach, D., 2007. Reconstruction of millennial changes in dust emission, transport and regional sea ice coverage using the deep EPICA ice cores from the Atlantic and Indian Ocean sector of Antarctica. Earth and Planetary Science Letters 260, 340–354. https://doi.org/10.1016/j.epsl.2007.06.014

Fontijn, K., Lachowycz, S.M., Rawson, H., Pyle, D.M., Mather, T.A., Naranjo, J.A., Moreno-Roa, H., 2014. Late Quaternary tephrostratigraphy of southern Chile and Argentina. Quaternary Science Reviews 89, 70–84. https://doi.org/10.1016/j.quascirev.2014.02.007

Fornace, K.L., Hughen, K.A., Shanahan, T.M., Fritz, S.C., Baker, P.A., Sylva, S.P., 2014. A 60,000-year record of hydrologic variability in the Central Andes from the hydrogen isotopic composition of leaf waxes in Lake Titicaca sediments. Earth and Planetary Science Letters 408, 263–271. https://doi.org/10.1016/j.epsl.2014.10.024

Gabrielli, P., Wegner, A., Petit, J.R., Delmonte, B., De Deckker, P., Gaspari, V., Fischer, H., Ruth, U., Kriews, M., Boutron, C., Cescon, P., Barbante, C., 2010. A major glacial-interglacial change in aeolian dust composition inferred from Rare Earth Elements in Antarctic ice. Quaternary Science Reviews 29, 265–273. https://doi.org/10.1016/j.quascirev.2009.09.002

Gaiero, D.M., 2007. Dust provenance in Antarctic ice during glacial periods: From where in southern South America? Geophysical Research Letters 34. https://doi.org/10.1029/2007GL030520

Gaiero, D.M., Depetris, P.J., Probst, J.-L., Bidart, S.M., Leleyter, L., 2004. The signature of river- and wind-borne materials exported from Patagonia to the southern latitudes: a view from REEs and implications for paleoclimatic interpretations. Earth and Planetary Science Letters 219, 357–376. https://doi.org/10.1016/S0012-821X(03)00686-1

Gaiero, D.M., Probst, J.-L., Depetris, P.J., Bidart, S.M., Leleyter, L., 2003. Iron and other transition metals in Patagonian riverborne and windborne materials: geochemical control and transport to the southern South Atlantic Ocean. Geochimica et Cosmochimica Acta 67, 3603–3623. https://doi.org/10.1016/S0016-7037(03)00211-4

Gaiero, D.M., Simonella, L., Gassó, S., Gili, S., Stein, A.F., Sosa, P., Becchio, R., Arce, J., Marelli, H., 2013. Ground/satellite observations and atmospheric modeling of dust storms originating in the high Puna-Altiplano deserts (South America): Implications for the interpretation of paleo-climatic archives. Journal of Geophysical Research: Atmospheres 118, 3817–3831. https://doi.org/10.1002/jgrd.50036

García, J.L., Kaplan, M.R., Hall, B.L., Schaefer, J.M., Vega, R.M., Schwartz, R., Finkel, R., 2012. Glacier expansion in southern Patagonia throughout the Antarctic cold reversal. Geology 40, 859–862. https://doi.org/10.1130/G33164.1

García, J.-L., Maldonado, A., de Porras, M.E., Nuevo Delaunay, A., Reyes, O., Ebensperger, C.A., Binnie, S.A., Lüthgens, C., Méndez, C., 2019. Early deglaciation and paleolake history of Río Cisnes Glacier, Patagonian Ice Sheet (44°S). Quaternary Research 91, 194–217. https://doi.org/10.1017/qua.2018.93

Gili, S., Gaiero, D.M., Goldstein, S.L., Chemale, F., Jweda, J., Kaplan, M.R., Becchio, R.A., Koester, E., 2017. Glacial/interglacial changes of Southern Hemisphere wind circulation from the geochemistry of South American dust. Earth and Planetary Science Letters 469, 98–109. https://doi.org/10.1016/j.epsl.2017.04.007

Gili, S., Vanderstraeten, A., Chaput, A., King, J., Gaiero, D.M., Delmonte, B., Vallelonga, P., Formenti, P., Di Biagio, C., Cazanau, M., Pangui, E., Doussin, J.-F., Mattielli, N., 2022. South African dust contribution to the high southern latitudes and East Antarctica during interglacial stages. Communications Earth & Environment 3, 129. https://doi.org/10.1038/s43247-022-00464-z

Gilli, A., Anselmetti, F.S., Ariztegui, D., Bradbury, J.P., Kelts, K.R., Markgraf, V., McKenzie, J.A., 2001. Tracking abrupt climate change in the Southern Hemisphere: a seismic stratigraphic study of Lago Cardiel, Argentina (49°S). Terra Nova 13, 443–448. https://doi.org/10.1046/j.1365-3121.2001.00377.x

Gingele, F.X., De Deckker, P., 2005. Clay mineral, geochemical and Sr–Nd isotopic fingerprinting of sediments in the Murray–Darling fluvial system, southeast Australia. Australian Journal of Earth Sciences 52, 965–974. https://doi.org/10.1080/08120090500302301

Glasser, N.F., Jansson, K.N., Duller, G.A.T., Singarayer, J., Holloway, M., Harrison, S., 2016. Glacial lake drainage in Patagonia (13-8 kyr) and response of the adjacent Pacific Ocean. Scientific Reports 6, 21064. https://doi.org/10.1038/srep21064

Grousset, F.E., Biscaye, P.E., 2005. Tracing dust sources and transport patterns using Sr, Nd and Pb isotopes. Chemical Geology 222, 149–167. https://doi.org/10.1016/j.chemgeo.2005.05.006

Grousset, F.E., Biscaye, P.E., Revel, M., Petit, J.-R., Pye, K., Joussaume, S., Jouzel, J., 1992. Antarctic (Dome C) ice-core dust at 18 k.y. B.P.: Isotopic constraints on origins. Earth and Planetary Science Letters 111, 175–182. https://doi.org/10.1016/0012-821X(92)90177-W

Haberle, S.G., Bennett, K.D., 2004. Postglacial formation and dynamics of North Patagonian Rainforest in the Chonos Archipelago, Southern Chile. Quaternary Science Reviews 23, 2433–2452. https://doi.org/10.1016/j.quascirev.2004.03.001

Haberzettl, T., Anselmetti, F.S., Bowen, S.W., Fey, M., Mayr, C., Zolitschka, B., Ariztegui, D., Mauz, B., Ohlendorf, C., Kastner, S., Lücke, A., Schäbitz, F., Wille, M., 2009. Late Pleistocene dust deposition in the Patagonian steppe - extending and refining the paleoenvironmental and tephrochronological record from Laguna Potrok Aike back to 55ka. Quaternary Science Reviews 28, 2927–2939. https://doi.org/10.1016/j.quascirev.2009.07.021

Henríquez, W.I., Villa-Martínez, R., Vilanova, I., De Pol-Holz, R., Moreno, P.I., 2017. The last glacial termination on the eastern flank of the central Patagonian Andes (47\degree\,S). Climate of the Past 13, 879–895. https://doi.org/10.5194/cp-13-879-2017

Hipondoka, M.H.T., Mauz, B., Kempf, J., Packman, S., Chiverrell, R.C., Bloemendal, J., 2014. Chronology of sand ridges and the Late Quaternary evolution of the Etosha Pan, Namibia. Geomorphology 204, 553–563. https://doi.org/10.1016/j.geomorph.2013.08.034

Huber, U.M., Markgraf, V., Schäbitz, F., 2004. Geographical and temporal trends in Late Quaternary fire histories of Fuego-Patagonia, South America. Quaternary Science Reviews 23, 1079–1097. https://doi.org/10.1016/j.quascirev.2003.11.002

Humphries, M.S., Benitez-Nelson, C.R., Bizimis, M., Finch, J.M., 2017. An aeolian sediment reconstruction of regional wind intensity and links to larger scale climate variability since the last deglaciation from the east coast of southern Africa. Global and Planetary Change 156, 59–67. https://doi.org/10.1016/j.gloplacha.2017.08.002

Kaplan, M.R., Fogwill, C.J., Sugden, D.E., Hulton, N.R.J., Kubik, P.W., Freeman, S.P.H.T., 2008. Southern Patagonian glacial chronology for the Last Glacial period and implications for Southern Ocean climate. Quaternary Science Reviews 27, 284–294. https://doi.org/10.1016/j.quascirev.2007.09.013

Kaplan, M.R., Schaefer, J.M., Denton, G.H., Barrell, D.J.A., Chinn, T.J.H., Putnam, A.E., Andersen, B.G., Finkel, R.C., Schwartz, R., Doughty, A.M., 2010. Glacier retreat in New Zealand during the Younger Dryas stadial. Nature 467, 194–197. https://doi.org/10.1038/nature09313

Koffman, B.G., Goldstein, S.L., Winckler, G., Borunda, A., Kaplan, M.R., Bolge, L., Cai, Y., Recasens, C., Koffman, T.N.B., Vallelonga, P., 2021. New Zealand as a source of mineral dust to the atmosphere and ocean. Quaternary Science Reviews 251, 106659. https://doi.org/10.1016/j.quascirev.2020.106659

Kurbatov, A.V., Zielinski, G.A., Dunbar, N.W., Mayewski, P.A., Meyerson, E.A., Sneed, S.B., Taylor, K.C., 2006. A 12,000 year record of explosive volcanism in the Siple Dome Ice Core, West Antarctica. Journal of Geophysical Research: Atmospheres 111. https://doi.org/10.1029/2005JD006072

Lambeck, K., Rouby, H., Purcell, A., Sun, Y., Sambridge, M., 2014. Sea level and global ice volumes from the Last Glacial Maximum to the Holocene. Proceedings of the National Academy of Sciences 111, 15296–15303. https://doi.org/10.1073/pnas.1411762111

Lambert, F., Delmonte, B., Petit, J.R., Bigler, M., Kaufmann, P.R., Hutterli, M.A., Stocker, T.F., Ruth, U., Steffensen, J.P., Maggi, V., 2008. Dust-climate couplings over the past 800,000 years from the EPICA Dome C ice core. Nature 452, 616–619. https://doi.org/10.1038/nature06763

Lambert, F., Opazo, N., Ridgwell, A., Winckler, G., Lamy, F., Shaffer, G., Kohfeld, K., Ohgaito, R., Albani, S., Abe-Ouchi, A., 2021. Regional patterns and temporal evolution of ocean iron fertilization and CO2 drawdown during the last glacial termination. Earth and Planetary Science Letters 554, 116675. https://doi.org/10.1016/j.epsl.2020.116675

Lambert, F., Tagliabue, A., Shaffer, G., Lamy, F., Winckler, G., Farias, L., Gallardo, L., De Pol-Holz, R., 2015. Dust fluxes and iron fertilization in Holocene and Last Glacial Maximum climates. Geophysical Research Letters 42, 6014–6023. https://doi.org/10.1002/2015GL064250

Lamy, F., Kaiser, J., Ninnemann, U., Hebbeln, D., Arz, H.W., Stoner, J., 2004. Antarctic Timing of Surface Water Changes off Chile and Patagonian Ice Sheet Response. Science 304, 1959–1962. https://doi.org/10.1126/science.1097863

Li, C., Sonke, J.E., Le Roux, G., Van der Putten, N., Piotrowska, N., Jeandel, C., Mattielli, N., Benoit, M., Wiggs, G.F.S., De Vleeschouwer, F., 2020. Holocene dynamics of the southern westerly winds over the Indian Ocean inferred from a peat dust deposition record. Quaternary Science Reviews 231, 106169. https://doi.org/10.1016/j.quascirev.2020.106169

Lim, S., Chase, B.M., Chevalier, M., Reimer, P.J., 2016. 50,000years of vegetation and climate change in the southern Namib Desert, Pella, South Africa. Palaeogeography, Palaeoclimatology, Palaeoecology 451, 197–209. https://doi.org/10.1016/j.palaeo.2016.03.001

Maher, B.A., Prospero, J.M., Mackie, D., Gaiero, D., Hesse, P.P., Balkanski, Y., 2010. Global connections between aeolian dust, climate and ocean biogeochemistry at the present day and at the last glacial maximum. Earth-Science Reviews 99, 61–97. https://doi.org/10.1016/j.earscirev.2009.12.001

Mancini, M.V., Franco, N.V., Brook, G.A., 2013. Palaeoenvironment and early human occupation of southernmost South America (South Patagonia, Argentina). Quaternary International 299, 13–22. https://doi.org/10.1016/j.quaint.2012.08.2056

Marino, F., Castellano, E., Nava, S., Chiari, M., Ruth, U., Wegner, A., Lucarelli, F., Udisti, R., Delmonte, B., Maggi, V., 2009. Coherent composition of glacial dust on opposite sides of the East Antarctic Plateau inferred from the deep EPICA ice cores. Geophysical Research Letters 36. https://doi.org/10.1029/2009GL040732

Markgraf, V., Bradbury, J.P., Schwalb, A., Burns, S.J., Stern, C., Ariztegui, D., Gilli, A., Anselmetti, F.S., Stine, S., Maidana, N., 2003. Holocene palaeoclimates of southern Patagonia: limnological and environmental history of Lago Cardiel, Argentina. The Holocene 13, 581–591. https://doi.org/10.1191/0959683603hl648rp

Markgraf, V., Webb, R.S., Anderson, K.H., Anderson, L., 2002. Modern pollen/climate calibration for southern South America. Palaeogeography, Palaeoclimatology, Palaeoecology 181, 375–397. https://doi.org/10.1016/S0031-0182(01)00414-X

Markgraf, V., Whitlock, C., Haberle, S., 2007. Vegetation and fire history during the last 18,000 cal yr B.P. in Southern Patagonia: Mallín Pollux, Coyhaique, Province Aisén (45°41′30″ S, 71°50′30″ W, 640 m elevation). Palaeogeography, Palaeoclimatology, Palaeoecology 254, 492–507. https://doi.org/10.1016/j.palaeo.2007.07.008

Markle, B.R., Steig, E.J., Roe, G.H., Winckler, G., McConnell, J.R., 2018. Concomitant variability in high-latitude aerosols, water isotopes and the hydrologic cycle. Nature Geoscience 11, 853–859. https://doi.org/10.1038/s41561-018-0210-9

Martínez-García, A., Sigman, D.M., Ren, H., Anderson, R.F., Straub, M., Hodell, D.A., Jaccard, S.L., Eglinton, T.I., Haug, G.H., 2014. Iron Fertilization of the Subantarctic Ocean During the Last Ice Age. Science 343, 1347–1350. https://doi.org/10.1126/science.1246848

Marx, S.K., Kamber, B.S., 2010. Trace-element systematics of sediments in the Murray–Darling Basin, Australia: Sediment provenance and palaeoclimate implications of fine scale chemical heterogeneity. Applied Geochemistry 25, 1221–1237. https://doi.org/10.1016/j.apgeochem.2010.05.007

Marx, S.K., Kamber, B.S., McGowan, H.A., 2005. Estimates of Australian dust flux into New Zealand: Quantifying the eastern Australian dust plume pathway using trace element calibrated 210Pb as a monitor. Earth and Planetary Science Letters 239, 336–351. https://doi.org/10.1016/j.epsl.2005.09.002

Masson, V., Vimeux, F., Jouzel, J., Morgan, V., Delmotte, M., Ciais, P., Hammer, C., Johnsen, S., Lipenkov, V.Ya., Mosley-Thompson, E., Petit, J.-R., Steig, E.J., Stievenard, M., Vaikmae, R., 2000. Holocene Climate Variability in Antarctica Based on 11 Ice-Core Isotopic Records. Quaternary Research 54, 348–358. https://doi.org/10.1006/qres.2000.2172

McCulloch, R.D., Bentley, M.J., Purves, R.S., Hulton, N.R.J., Sugden, D.E., Clapperton, C.M., 2000. Climatic inferences from glacial and palaeoecological evidence at the last glacial termination, southern South America. Journal of Quaternary Science 15, 409–417. https://doi.org/10.1002/1099-1417(200005)15:4<409::AID-JQS539>3.0.CO;2-#

McGowan, H.A., Kamber, B., McTainsh, G.H., Marx, S.K., 2005. High resolution provenancing of long travelled dust deposited on the Southern Alps, New Zealand. Geomorphology 69, 208–221. https://doi.org/10.1016/j.geomorph.2005.01.005

Monteath, A., Hughes, P., Cooper, M., Groff, D., Scaife, R., Hodgson, D., 2022. Late glacial–Holocene record of Southern Hemisphere westerly wind dynamics from the Falkland Islands, South Atlantic Ocean. Geology 50, 880–885. https://doi.org/10.1130/G49805.1

Moreno, P.I., Denton, G.H., Moreno, H., Lowell, T.V., Putnam, A.E., Kaplan, M.R., 2015. Radiocarbon chronology of the last glacial maximum and its termination in northwestern Patagonia. Quaternary Science Reviews 122, 233–249. https://doi.org/10.1016/j.quascirev.2015.05.027

Moreno, P.I., Kaplan, M.R., François, J.P., Villa-Martínez, R., Moy, C.M., Stern, C.R., Kubik, P.W., 2009. Renewed glacial activity during the Antarctic cold reversal and persistence of cold conditions until 11.5 ka in southwestern Patagonia. Geology 37, 375–378. https://doi.org/10.1130/G25399A.1

Moreno, P.I., Videla, J., Valero-Garcés, B., Alloway, B.V., Heusser, L.E., 2018. A continuous record of vegetation, fire-regime and climatic changes in northwestern Patagonia spanning the last 25,000 years. Quaternary Science Reviews 198, 15–36. https://doi.org/10.1016/j.quascirev.2018.08.013

Neff, P.D., Bertler, N.A.N., 2015. Trajectory modeling of modern dust transport to the Southern Ocean and Antarctica. Journal of Geophysical Research: Atmospheres 120, 9303–9322. https://doi.org/10.1002/2015JD023304

Pedro, J.B., Bostock, H.C., Bitz, C.M., He, F., Vandergoes, M.J., Steig, E.J., Chase, B.M., Krause, C.E., Rasmussen, S.O., Markle, B.R., Cortese, G., 2016. The spatial extent and dynamics of the Antarctic Cold Reversal. Nature Geoscience 9, 51–55. https://doi.org/10.1038/ngeo2580

Pendall, E., Markgraf, V., White, J.W.C., Dreier, M., Kenny, R., 2001. Multiproxy Record of Late Pleistocene–Holocene Climate and Vegetation Changes from a Peat Bog in Patagonia. Quaternary Research 55, 168–178. https://doi.org/10.1006/qres.2000.2206

Petherick, L., McGowan, H., Moss, P., 2008. Climate variability during the Last Glacial Maximum in eastern Australia: evidence of two stadials? Journal of Quaternary Science 23, 787–802. https://doi.org/10.1002/jqs.1186

Petherick, L.M., McGowan, H.A., Kamber, B.S., 2009. Reconstructing transport pathways for late Quaternary dust from eastern Australia using the composition of trace elements of long traveled dusts. Geomorphology 105, 67–79. https://doi.org/10.1016/j.geomorph.2007.12.015

Pichevin, L., Cremer, M., Giraudeau, J., Bertrand, P., 2005. A 190 ky record of lithogenic grain-size on the Namibian slope: Forging a tight link between past wind-strength and coastal upwelling dynamics. Marine Geology 218, 81–96. https://doi.org/10.1016/j.margeo.2005.04.003

Placzek, C., Quade, J., Patchett, P.J., 2006. Geochronology and stratigraphy of late Pleistocene lake cycles on the southern Bolivian Altiplano: Implications for causes of tropical climate change. GSA Bulletin 118, 515–532. https://doi.org/10.1130/B25770.1

Qu, Z., 2016. Chemical properties of continental aerosol transported over the Southern Ocean : Patagonian and Namibian sources (Ph.D. Thesis). Université Pierre et Marie Curie - Paris VI, Paris.

Quade, J., Kaplan, M.R., 2017. Lake-level stratigraphy and geochronology revisited at Lago (Lake) Cardiel, Argentina, and changes in the Southern Hemispheric Westerlies over the last 25 ka. Quaternary Science Reviews 177, 173–188. https://doi.org/10.1016/j.quascirev.2017.10.006

Ram, M., Gayley, R.I., Petit, J.-R., 1988. Insoluble particles in Antarctic ice: Background aerosol size distribution and diatom concentration. Journal of Geophysical Research: Atmospheres 93, 8378–8382. https://doi.org/10.1029/JD093iD07p08378

Reboita, M.S., Nieto, R., da Rocha, R.P., Drumond, A., Vázquez, M., Gimeno, L., 2019. Characterization of Moisture Sources for Austral Seas and Relationship with Sea Ice Concentration. Atmosphere 10. https://doi.org/10.3390/atmos10100627

Revel-Rolland, M., De Deckker, P., Delmonte, B., Hesse, P.P., Magee, J.W., Basile-Doelsch, I., Grousset, F., Bosch, D., 2006. Eastern Australia: A possible source of dust in East Antarctica interglacial ice. Earth and Planetary Science Letters 249, 1–13. https://doi.org/10.1016/j.epsl.2006.06.028

Rudnick, R.L., Gao, S., 2003. 3.01 - Composition of the Continental Crust, in: Holland, H.D., Turekian, K.K. (Eds.), Treatise on Geochemistry. Pergamon, Oxford, pp. 1–64. https://doi.org/10.1016/B0-08-043751-6/03016-4

Ruth, U., Barbante, C., Bigler, M., Delmonte, B., Fischer, H., Gabrielli, P., Gaspari, V., Kaufmann, P., Lambert, F., Maggi, V., Marino, F., Petit, J.-R., Udisti, R., Wagenbach, D., Wegner, A., Wolff, E.W., 2008. Proxies and Measurement Techniques for Mineral Dust in Antarctic Ice Cores. Environ. Sci. Technol. 42, 5675–5681. https://doi.org/10.1021/es703078z

Shi, N., Dupont, L.M., Beug, H.-J., Schneider, R., 1998. Vegetation and climate changes during the last 21 000 years in S.W. Africa based on a marine pollen record. Vegetation History and Archaeobotany 7, 127–140. https://doi.org/10.1007/BF01374001

Shi, N., Schneider, R., Beug, H.-J., Dupont, L.M., 2001. Southeast trade wind variations during the last 135 kyr: evidence from pollen spectra in eastern South Atlantic sediments. Earth and Planetary Science Letters 187, 311–321. https://doi.org/10.1016/S0012-821X(01)00267-9

Shi, Z., Krom, M.D., Bonneville, S., Baker, A.R., Bristow, C., Drake, N., Mann, G., Carslaw, K., McQuaid, J.B., Jickells, T., Benning, L.G., 2011. Influence of chemical weathering and aging of iron oxides on the potential iron solubility of Saharan dust during simulated atmospheric processing. Global Biogeochemical Cycles 25. https://doi.org/10.1029/2010GB003837

Shulmeister, J., Thackray, G.D., Rittenour, T.M., Hyatt, O.M., 2018. Multiple glacial advances in the Rangitata Valley, South Island, New Zealand, imply roles for Southern Hemisphere westerlies and summer insolation in MIS 3 glacial advances. Quaternary Research 89, 375–393. https://doi.org/10.1017/qua.2017.108

Skirrow, G.K., Smedley, R.K., Chiverrell, R.C., Hooke, J.M., 2021. Planform change of the Río Chubut (~42°S, ~70°W, Argentina) in response to climate drivers in the southern Andes. Geomorphology 393, 107924. https://doi.org/10.1016/j.geomorph.2021.107924

Stenni, B., Masson-Delmotte, V., Selmo, E., Oerter, H., Meyer, H., Röthlisberger, R., Jouzel, J., Cattani, O., Falourd, S., Fischer, H., Hoffmann, G., Iacumin, P., Johnsen, S.J., Minster, B., Udisti, R., 2010. The deuterium excess records of EPICA Dome C and Dronning Maud Land ice cores (East Antarctica). Quaternary Science Reviews 29, 146–159. https://doi.org/10.1016/j.quascirev.2009.10.009

Sugden, D.E., McCulloch, R.D., Bory, A.J.-M., Hein, A.S., 2009. Influence of Patagonian glaciers on Antarctic dust deposition during the last glacial period. Nature Geoscience 2, 281–285. https://doi.org/10.1038/ngeo474

Sutherland, J.L., Carrivick, J.L., Evans, D.J.A., Shulmeister, J., Quincey, D.J., 2019. The Tekapo Glacier, New Zealand, during the Last Glacial Maximum: An active temperate glacier influenced by intermittent surge activity. Geomorphology 343, 183–210. https://doi.org/10.1016/j.geomorph.2019.07.008

Thomas, D.S.G., Brook, G., Shaw, P., Bateman, M., Haberyan, K., Appleton, C., Nash, D., McLaren, S., Davies, F., 2003. Late Pleistocene wetting and drying in the NW Kalahari: an integrated study from the Tsodilo Hills, Botswana. Quaternary International 104, 53–67. https://doi.org/10.1016/S1040-6182(02)00135-0

Thomas, D.S.G., Shaw, P.A., 2002. Late Quaternary environmental change in central southern Africa: new data, synthesis, issues and prospects. Quaternary Science Reviews 21, 783–797. https://doi.org/10.1016/S0277-3791(01)00127-5

Thorndycraft, V.R., Bendle, J.M., Benito, G., Davies, B.J., Sancho, C., Palmer, A.P., Fabel, D., Medialdea, A., Martin, J.R.V., 2019. Glacial lake evolution and Atlantic-Pacific drainage reversals during deglaciation of the Patagonian Ice Sheet. Quaternary Science Reviews 203, 102–127. https://doi.org/10.1016/j.quascirev.2018.10.036

Torre, G., Gaiero, D., Coppo, R., Cosentino, N.J., Goldstein, S.L., De Vleeschouwer, F., Roux, G.L., Bolge, L., Kiro, Y., Sawakuchi, A.O., 2022. Unraveling late Quaternary atmospheric circulation in the Southern Hemisphere through the provenance of Pampean loess. Earth-Science Reviews 232, 104143. https://doi.org/10.1016/j.earscirev.2022.104143

Tozer, B., Sandwell, D.T., Smith, W.H.F., Olson, C., Beale, J.R., Wessel, P., 2019. Global Bathymetry and Topography at 15 Arc Sec: SRTM15+. Earth and Space Science 6, 1847–1864. https://doi.org/10.1029/2019EA000658

Villa-Martínez, R., Moreno, P.I., 2021. Development and resilience of deciduous Nothofagus forests since the Last Glacial Termination and deglaciation of the central Patagonian Andes.

Palaeogeography, Palaeoclimatology, Palaeoecology 574, 110459. https://doi.org/10.1016/j.palaeo.2021.110459

Wagner, R., Schepanski, K., Klose, M., 2021. The Dust Emission Potential of Agricultural-Like Fires—Theoretical Estimates From Two Conceptually Different Dust Emission Parameterizations. Journal of Geophysical Research: Atmospheres 126, e2020JD034355. https://doi.org/10.1029/2020JD034355

Weber, M.E., Clark, P.U., Kuhn, G., Timmermann, A., Sprenk, D., Gladstone, R., Zhang, X., Lohmann, G., Menviel, L., Chikamoto, M.O., Friedrich, T., Ohlwein, C., 2014. Millennial-scale variability in Antarctic ice-sheet discharge during the last deglaciation. Nature 510, 134–138. https://doi.org/10.1038/nature13397

Weber, M.E., Kuhn, G., Sprenk, D., Rolf, C., Ohlwein, C., Ricken, W., 2012. Dust transport from Patagonia to Antarctica – A new stratigraphic approach from the Scotia Sea and its implications for the last glacial cycle. Quaternary Science Reviews 36, 177–188. https://doi.org/10.1016/j.quascirev.2012.01.016

Wegner, A., Fischer, H., Delmonte, B., Petit, J.-R., Erhardt, T., Ruth, U., Svensson, A., Vinther, B., Miller, H., 2015. The role of seasonality of mineral dust concentration and size on glacial/interglacial dust changes in the EPICA Dronning Maud Land ice core. Journal of Geophysical Research: Atmospheres 120, 9916–9931. https://doi.org/10.1002/2015JD023608

Wegner, A., Gabrielli, P., Wilhelms-Dick, D., Ruth, U., Kriews, M., De Deckker, P., Barbante, C., Cozzi, G., Delmonte, B., Fischer, H., 2012. Change in dust variability in the Atlantic sector of Antarctica at the end of the last deglaciation. Climate of the Past 8, 135–147. https://doi.org/10.5194/cp-8-135-2012

Whitlock, C., Moreno, P.I., Bartlein, P., 2007. Climatic controls of Holocene fire patterns in southern South America. Quaternary Research 68, 28–36. https://doi.org/10.1016/j.yqres.2007.01.012

Williams, P.W., McGlone, M., Neil, H., Zhao, J.-X., 2015. A review of New Zealand palaeoclimate from the Last Interglacial to the global Last Glacial Maximum. Quaternary Science Reviews 110, 92–106. https://doi.org/10.1016/j.quascirev.2014.12.017

List of Supplementary materials

Supplementary text: *Laboratory method and analyses*

Supplementary text: *Effect of initialization conditions (i.e. order of DS) in the REE input database on % contributions*

Fig S1: Localization of dust sources (DS) used in our apportionment model.

Fig. S2: REE patterns of all the Dust Source (DS) assembled by PSA

Fig S3: Examples of modelled fit to REE pattern in EDML ice core.

Fig S4: Example of distributions of % contributions of DS “PataGi4”.

Fig S5: Aggregated density probability function per PSA.

Fig S6: Number of DS involved in the dust assemblage through time and histogram of R median values.

Fig S7: Variability of % PSA contributions for successive runs of model and for different order of DS in the REE database.

Fig S8: Maps of emerged shelves in PAT and S-NZ over time through the LGIT.

Table S1: Correction factor (*cf*) and error applied to EDML samples.

Table S2: Description of Dust Sources (DS) included in the apportionment model.

Table S3: Model outputs for the 396 samples.

Table S4: Isotopic composition and Sr and Nd concentrations of PSA.

Supplementary Information

Laboratory method and analyses

Regarding PSA samples compilation, our study relies mostly on literature data ((Gaiero et al., 2004) ; (Marx et al., 2005); (McGowan et al., 2005); (Marx and Kamber, 2010) ; (Gili et al., 2017); (Li et al., 2020); (Koffman et al., 2021)). Yet, data from Southern Africa (SAF) are sparse, only six aerosol samples were available (Li et al., 2020). Thus, we analyzed the REE contents in 11 additional topsoil samples collected in (Gili et al., 2022) from the Namibian coast at Kuiseb, Omaruru and Huab river bed sediments. The fine fraction (*i.e.*, < 5µm particles) was extracted and REE analysis were conducted at the G-Time laboratory at ULB.

To avoid contamination, the sample preparation and chemical analysis were performed in a laminar flow hood (Class 100) within a Class 1000 laboratory. The reagents *i.e.*, 6 mol L^{-1} HCl, 14 mol L^{-1} HNO_3 and 23 mol L^{-1} HF (Merck®, pro-analis) - were systematically purified via distillation and sub-boiling before use. MilliQ water (18.2 M Ω.cm) was also used at all steps. All analytical procedures took place under the cleanest conditions using acid-cleaned Savillex® or Teflon vials, acid-cleaned uncoloured tips and powder-free gloves to prevent any contamination.

After careful weighting, the < 5µm fraction was dissolved in 1.5 mL of 14 M HNO_3 and 0.5 mL of 23 M HF on a hot plate at 120 °C for 48h. The solution was dried down on a hot plate at 90 °C before addition of 2 mL of 6 M HCl and re-dissolved for 24 hours at 120 °C. Samples were dried down again before appropriate dilution for ICP-MS analysis. The REE content was determined on an Agilent 7700 ICP-mass spectrometer. Following sample digestion and addition of indium (In) as an internal standard and adequate dilution, REE (from La to Lu) were measured. Quantification took place against an external calibration curve, while oxide production was evaluated and corrected using particular combinations of single-element standard solutions. The blank levels had no significant effect on the calculated sample concentrations. Next to the samples, replicates, blanks, international reference basalt BHVO-2 and andesite AGV-2 of the U.S. Geological Survey with certified compositions were processed in the same way and used to evaluate the accuracy and precision of the analytical procedure. Based on repeated measurements of these rock standards, the analytical precision of the procedure outlined above is estimated to be below 3.5% relative standard deviation (%RSD). The obtained REE concentrations for these reference materials agree within uncertainty (1 standard deviation) with those certified, in other words, show a relative difference >1%.

Effect of initialization conditions of the REE input database on the model output.

Initialization conditions (i.e., the order of 207 DS in the input matrix in Eq.3) have been reported in the literature to have an influence on the solution and convergence rate of iterative algorithms such as the one at the basis of the *lsqnonneg* routine (Fathi Hafshejani and Moaberfard, 2022). A potential issue would come from the fact that the algorithm might find a local minimum after a given number of iterations regardless of the "fitting value" of the DS used. Thus, for a given order of DS in the input matrix, this artefact would create a positive bias towards a certain set of DS unrepresentative of their actual contributions to the REE mix but only as a calculation artefact. To investigate this issue (i.e. the sensibility of our results to the set-up of our input matrix), we performed (i) a run of the model with an input matrix for which the order of DS was permuted and (ii) two successive runs of the model with the same, non-permuted matrix. All model runs were done with 5000 Monte Carlo simulations. The non-permutated matrix is the one used originally in the model to produce the results presented here in which DS are ranked as follow: PAT (DS_{1} to DS_{39}), CWA (DS_{40} to DS_{44}), PAP (DS_{45} to DS_{58}), SAF (DS_{59} to DS_{75}), AUS (DS_{76} to DS_{182}), NZ (DS_{183} to DS_{207}). The permuted matrix has the DS of PAT permuted to the last position of the input matrix as described here: CWA (DS_{1} to DS_{4}), PAP (DS_{5} to DS_{18}), SAF (DS_{19} to DS_{35}), AUS (DS_{36} to DS_{142}), NZ (DS_{143} to DS_{167}), PAT (DS_{168} to DS_{207}). This experiment allows (i) to visualize the variability in the outputs between two successive runs of the model set-up with the same initialization conditions and (ii) to compare it with the variability of the model outputs induced by changes in the initial conditions. Fig. R25 (bottom) shows that the variability between successive runs of model with the non-permuted input matrix is very limited especially considering the 5000 Monte Carlo simulations. With respect to the output variability caused by the initialization conditions, Fig. S7 (top) clearly demonstrates that the order of DS of the input matrix has no significant effect on the results of the model. In addition, there is no increase in the residuals (i.e. difference between the contributions of a given DS for a given timestep) between the two sets of simulations (i.e., using permuted or non-permuted matrices), showing that initial conditions do not influence our results or create bias in favor of certain DS based on their position in the input matrix.

Similarly, we also investigated whether the number of DS per PSA has an influence on their output. We have tested this potential bias along the development of the database of REE patterns for New Zealand and Australia. In a first stage, our input database for New Zealand was limited to 6 DS from

Marx et al., (2005), which were complemented at a later stage with an extra 19 DS patterns from Koffman et al. (2021). Yet, the outputs of the model for New Zealand with 6 and 25 REE patterns were close. For Australia, we started with 51 REE patterns (mostly from Darling Basin and Lake Eyre) and later added Murray Basin and other nearby areas from Marx and Kamber, (2010) for a total of 107 REE patterns. Again, this increase did not change much Australian contributions. This shows that our database includes REE pattern representative of the source of dust to EDML and that the % contributions of a given PSA does not depend much on the number of DS associated to this particular PSA.

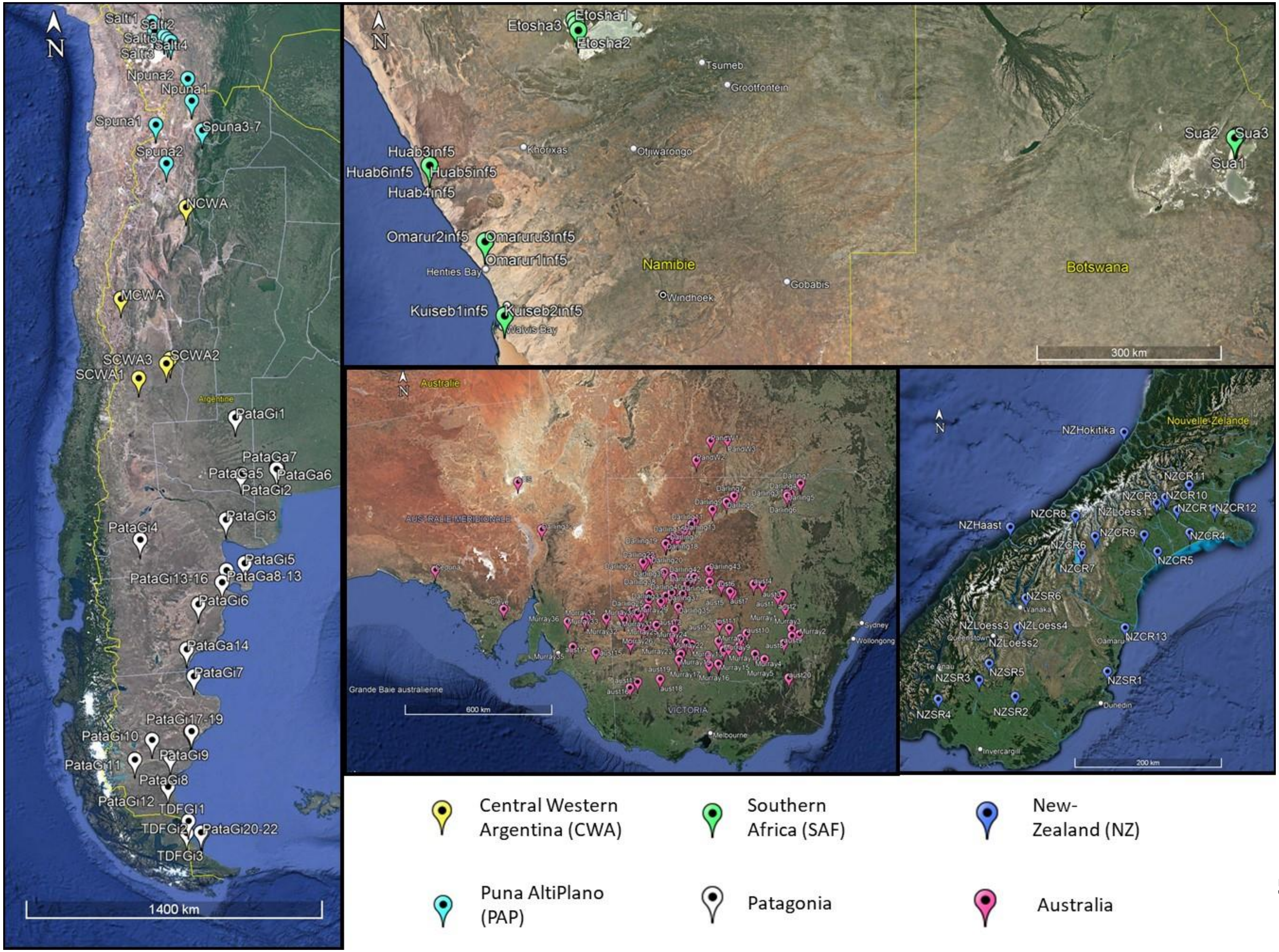
N
Salti1
Salti2
Salti5
Salti4
Salti3
Npuna2
Npuna1
Spuna1
Spuna3-7
Spuna2
NCWA
MCWA
SCWA3
SCWA2
SCWA1
Argentine
PataGi1
PataGa7
PataGa5
PataGa6
PataGi2
PataGi3
PataGi4
PataGi5
PataGi13-16
PataGa8-13
PataGi6
PataGa14
PataGi7
PataGi17-19
PataGi10
PataGi9
PataGi11
PataGi8
PataGi12
TDFGI1
TDFGi2
PataGi20-22
TDFGi3
1400 km
Etosha1
Etosha3
Etosha2
Tsumeb
Grootfontein
Sua2
Sua3
Sua1
Huab3inf5
Huab6inf5
Huab5inf5
Huab4inf5
Khorixas
Otjiwarongo
Omarur2inf5
Omaruru3inf5
Omarur1inf5
Henties Bay
Namibie
Botswana
Windhoek
Gobabis
Kuiseb1inf5
Kuiseb2inf5
Walvis Bay
300 km
Australie
AUSTRALIE-MÉRIDIONALE
Grande Baie australienne
600 km
VICTORIA
Melbourne
Sydney
Wollongong
Nouvelle-Zélande
NZHokitika
NZCR11
NZCR3
NZCR10
NZCR8
NZLoess1
NZCR1
NZCR12
NZHaast
NZCR6
NZCR9
NZCR4
NZCR7
NZCR5
NZSR6
Wanaka
NZLoess3
NZLoess4
Queenstown
NZLoess2
Oamaru
NZCR13
Te Anau
NZSR3
NZSR5
NZSR1
NZSR4
NZSR2
Dunedin
Invercargill
200 km
Central Western Argentina (CWA)
Southern Africa (SAF)
New-Zealand (NZ)
Puna AltiPlano (PAP)
Patagonia
Australia

Figure S1: Localization of dust sources (DS) used in our apportionment model in South America (including Patagonia, Central Western Argentina and Puna-Altiplano), Southern Africa, South-Eastern Australia and South-Island in New Zealand (see Table S2 for details).

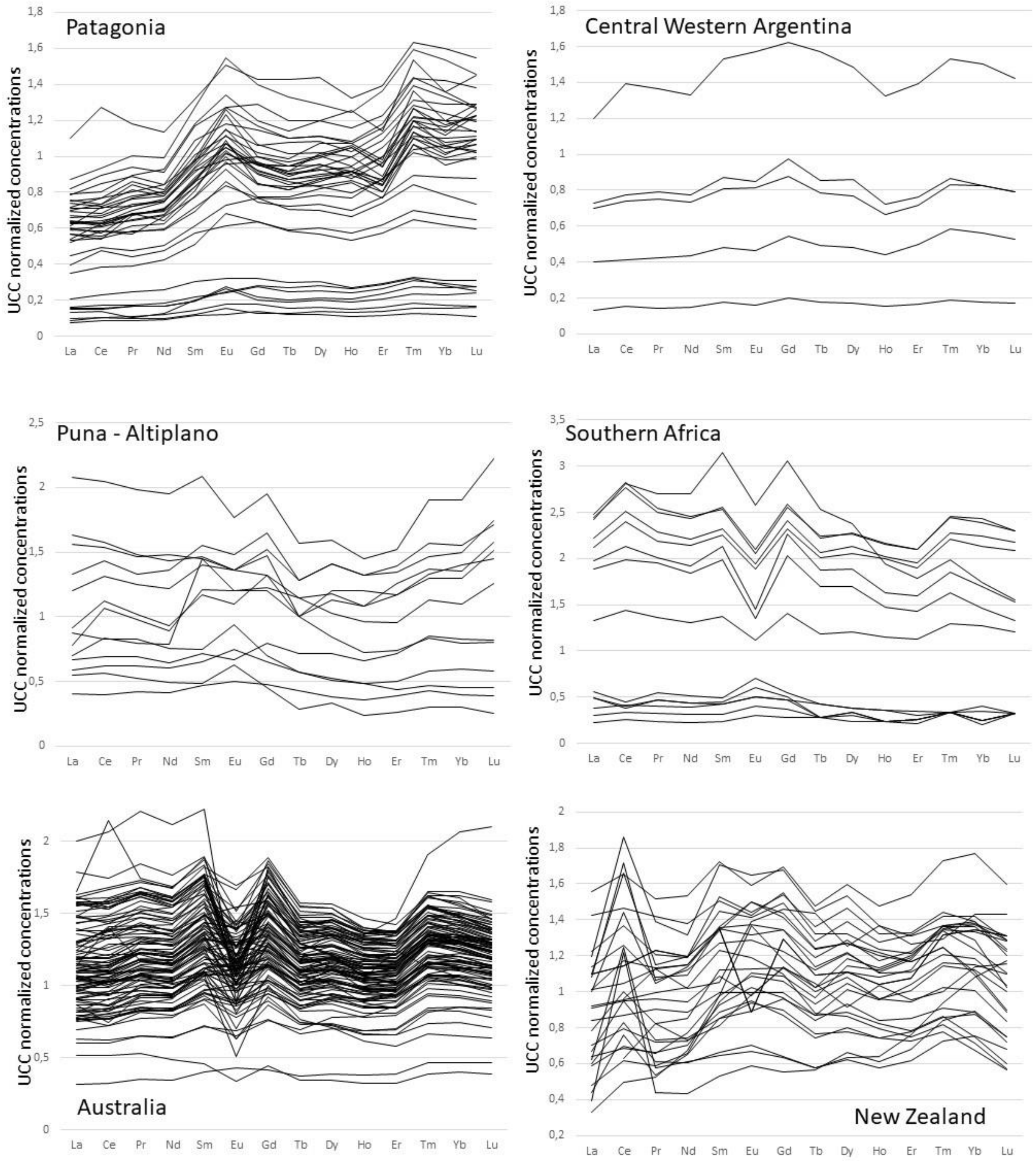

Figure S2: REE patterns of all the Dust Source (DS) assembled by PSA. All the concentrations are normalized to UCC (Rodnick et al. 2003).

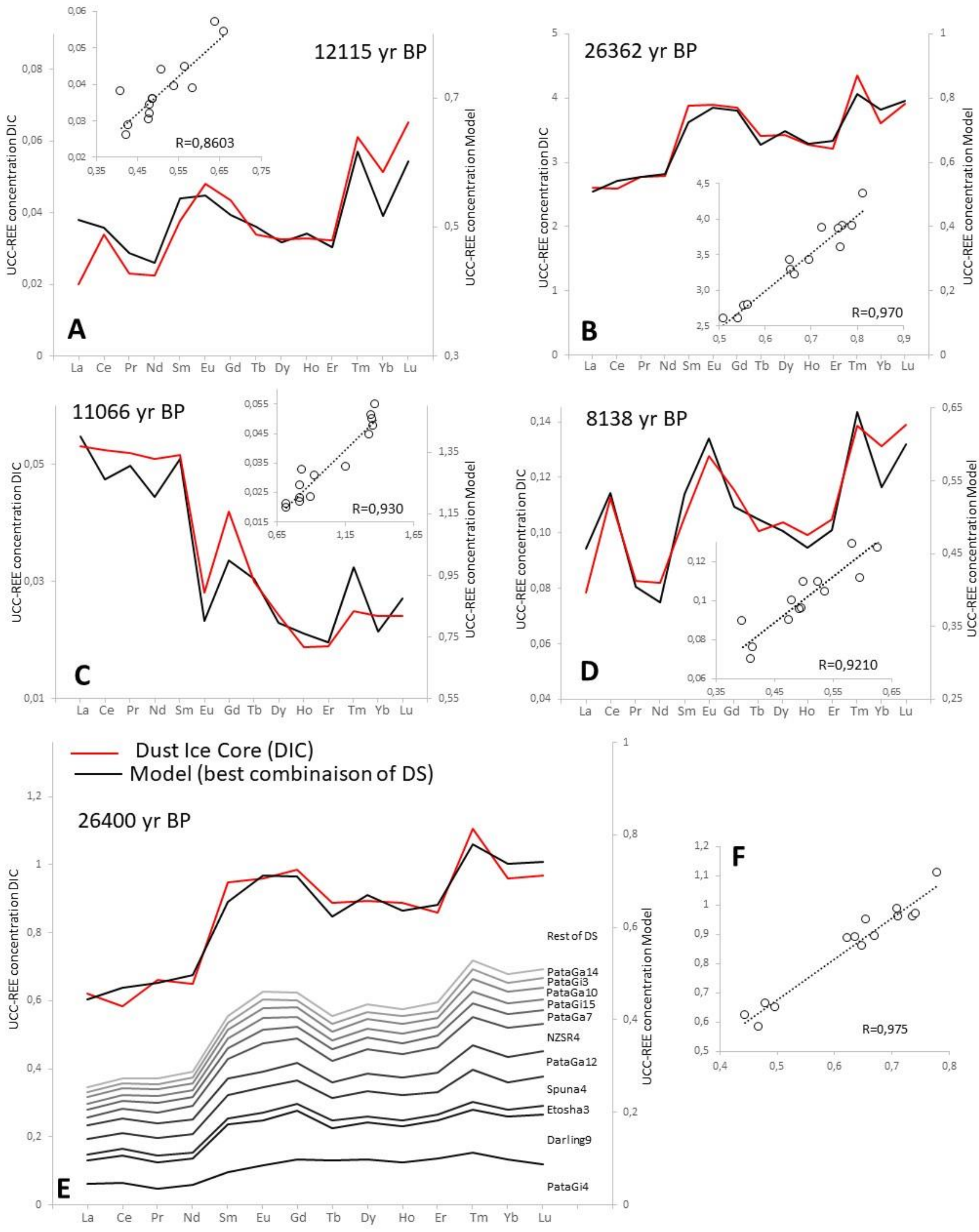

*Figure S3: (**A**), (**B**), (**C**), (**D**), (**E**) illustrates some examples of modelled fits (over 5000 MC simulations) compared to their corresponding Dust Ice Core REE pattern (see Table S2) and the associated correlation factor R (inserts). (**E**) illustrates of the cumulated individual contributions of the DS for the modelled fit to the DIC at 26400 kyr BP. Note that all those individual DS contributions are later aggregated by PSA for each time-step.*

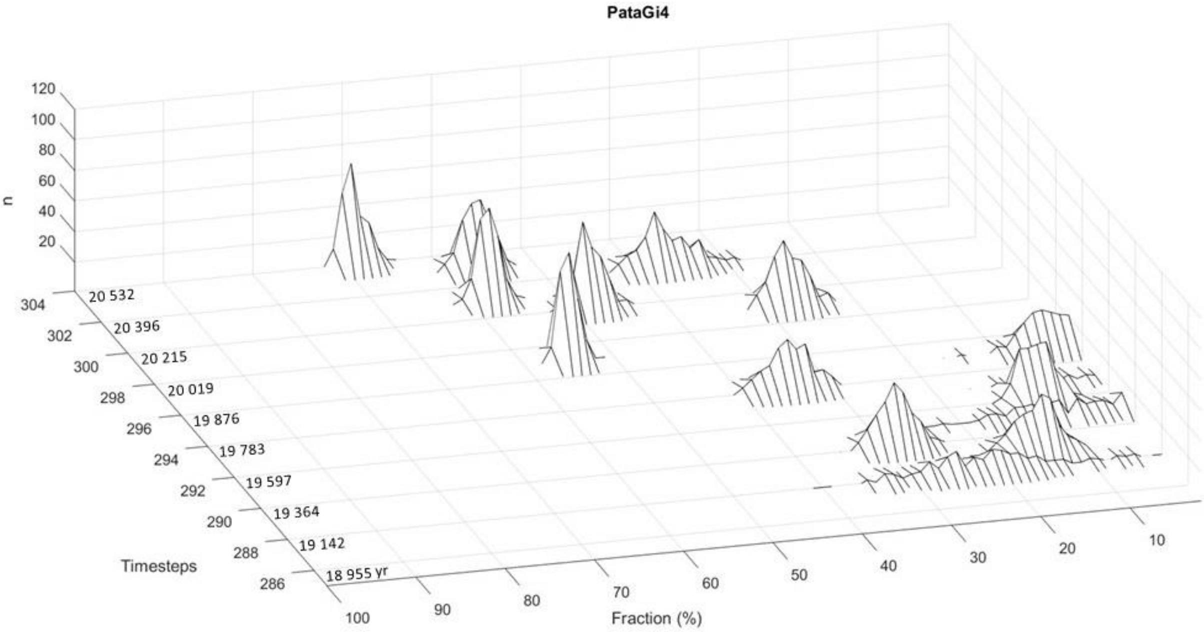

Fig S4: Illustration of distributions of % contributions of DS "PataGi4" (see Table S2) between 18 955 (step 286) and 20 532 yr BP (step 304) for 1000 MC iterations. n denotes the number of iterations for which the DS appears at a given % contribution in the dust mixture.

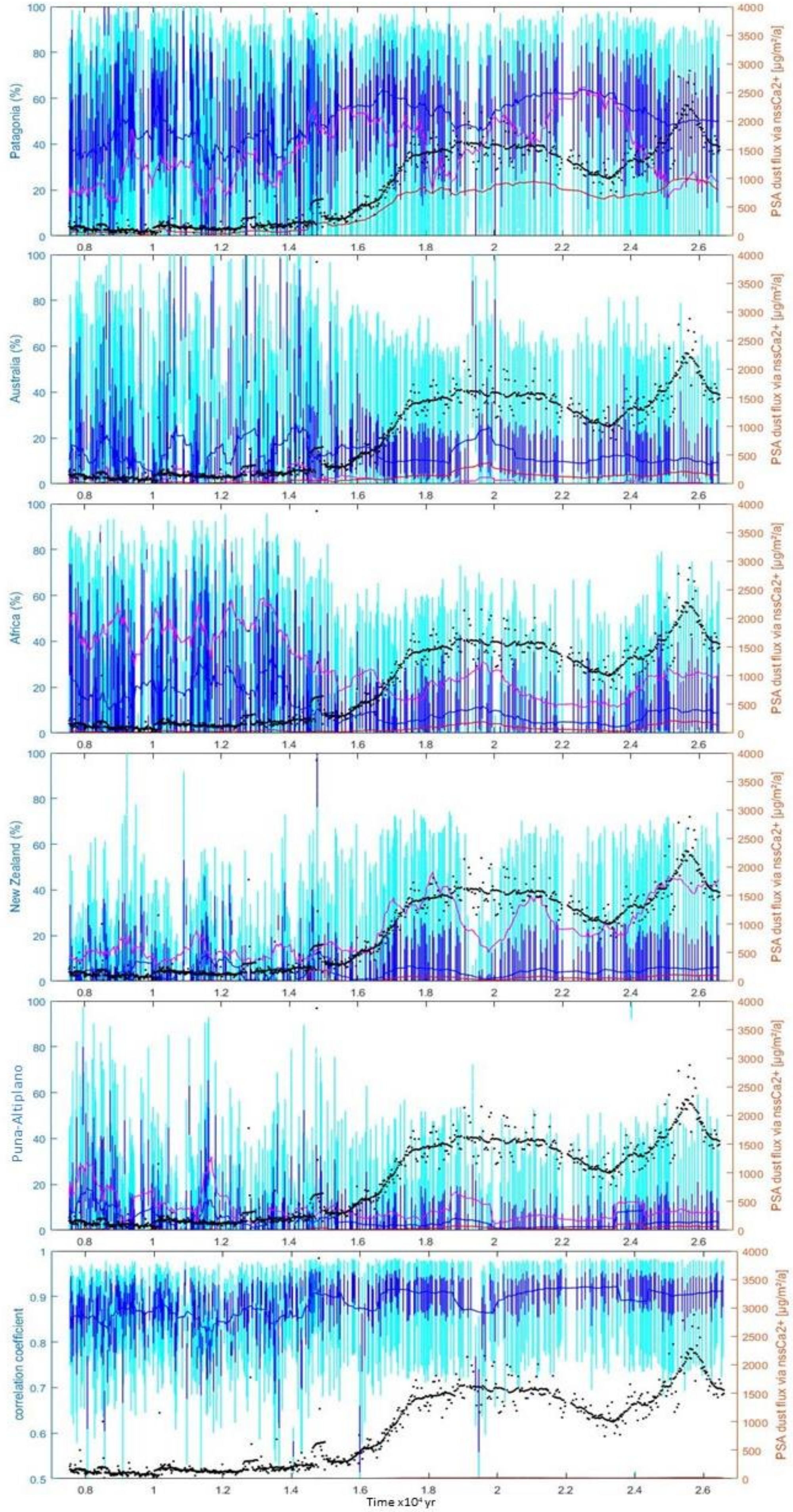

Patagonia (%)
Australia (%)
Africa (%)
New Zealand (%)
Puna-Altiplano
correlation coefficient
PSA dust flux via nssCa2+ [µg/m²/a]
Time x10⁴ yr

Fig S5: Aggregated density probability function per PSA. From top to bottom: Patagonia, Australia, Southern Africa, New-Zealand (South Island), Puna-Altiplano and coefficient of correlation R (Eq. 4). Vertical light blue dots are the results of the 5000 MC iterations for each time- step aggregated per PSA. Those MC iterations form a distribution (see Fig. S2) from which we extract the 95% confidence interval (vertical dark blue dots). The median of the latter interval is used then as a quantification of the % contribution of the PSA for this timestep to EDML total deposition. Here, the median values are represented by the 9-timesteps mobile average (dark blue line). The black dots denote the total dust flux (as nss Ca^{2+}) to EDML (data from Fischer et al. 2007). The pink line represents the flux of dust (9-timesteps mobile average) deposited at EDML in the provenance of the given PSA (i.e., the product of the % contribution and total dust flux).

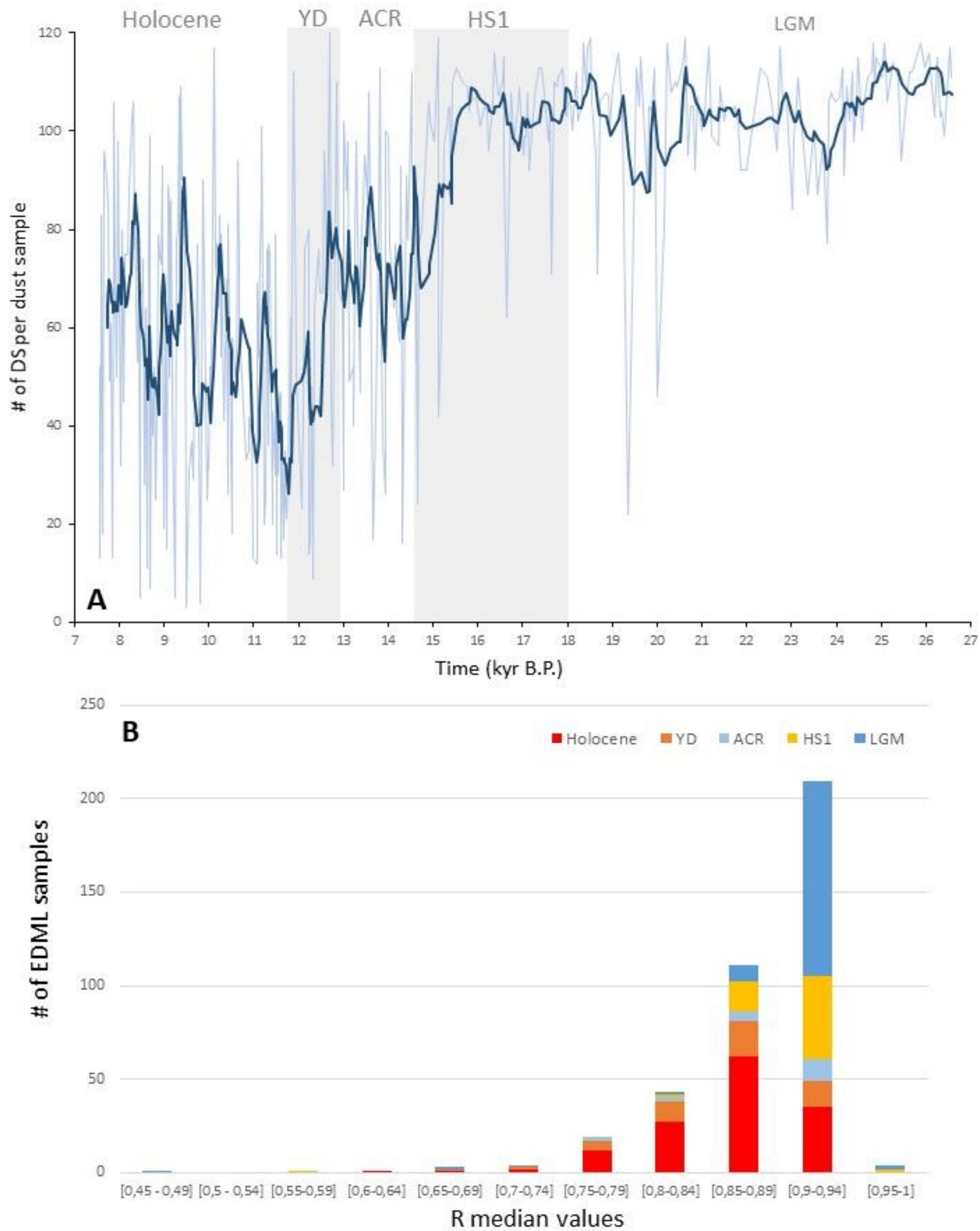

*Figure S6: (**A**) Number of DS (out of 207) involved in the fit of each dust ice core (DIC) sample over the last glacial-interglacial transition. (**B**) Histogram of R median value for the 396 EDMl samples. Note that for our reconstruction we rejected the samples that had R median values < 0.67 (99% confidence interval, p-value <0.01*).

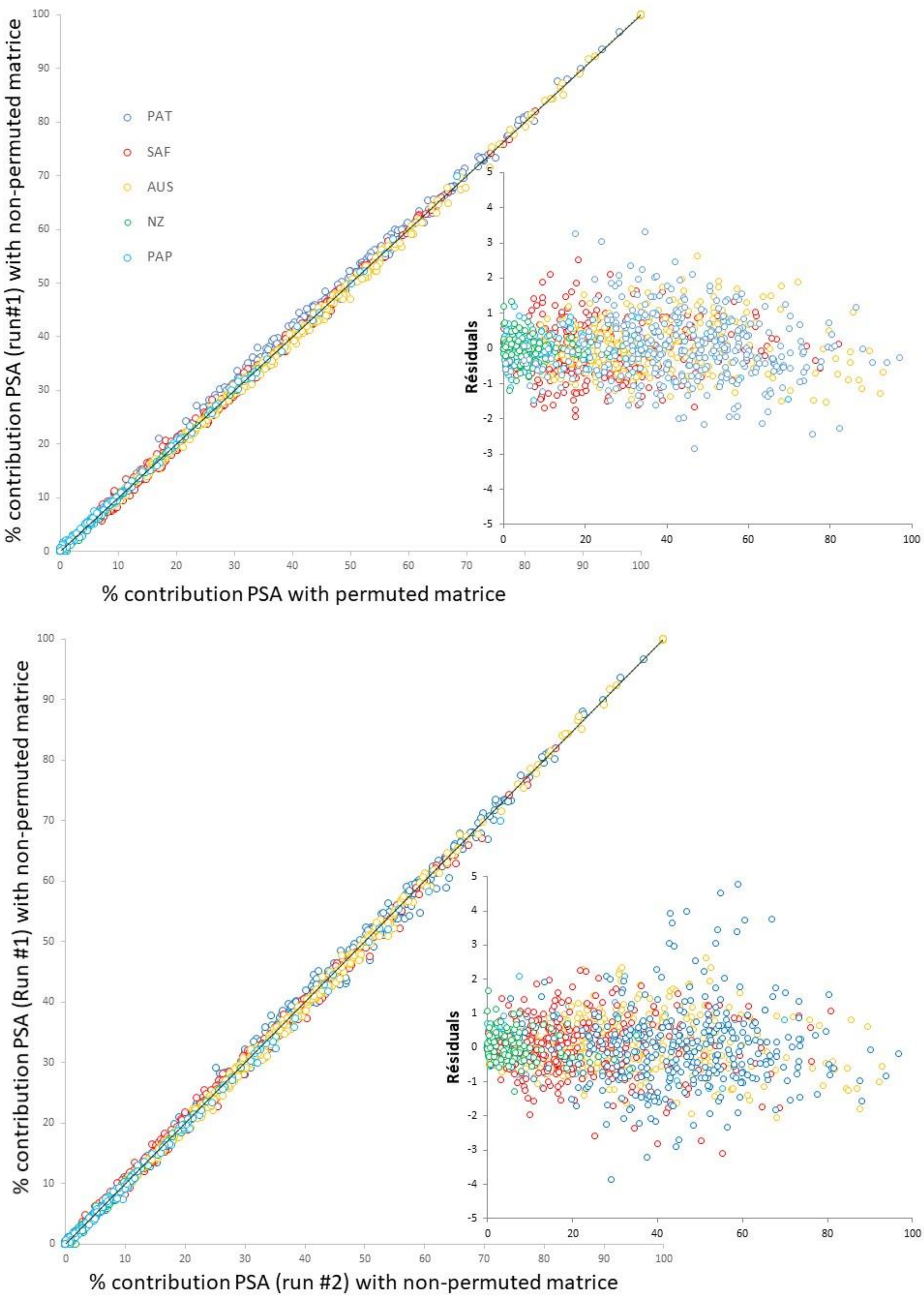

Figure S7 (Top) % PSA contribution in model run with DS in permuted order vs. % PSA contribution in model run with DS in non-permuted order of DS (i.e. order DS of the original model run). (Bottom) shows the two successive runs of the model with the non-permuted order of DS in the input matrice. Solid line denotes the 1:1 line. The different color refers to the various PSA. Insert graphs shows the residuals plot of the regressions for each PSA.

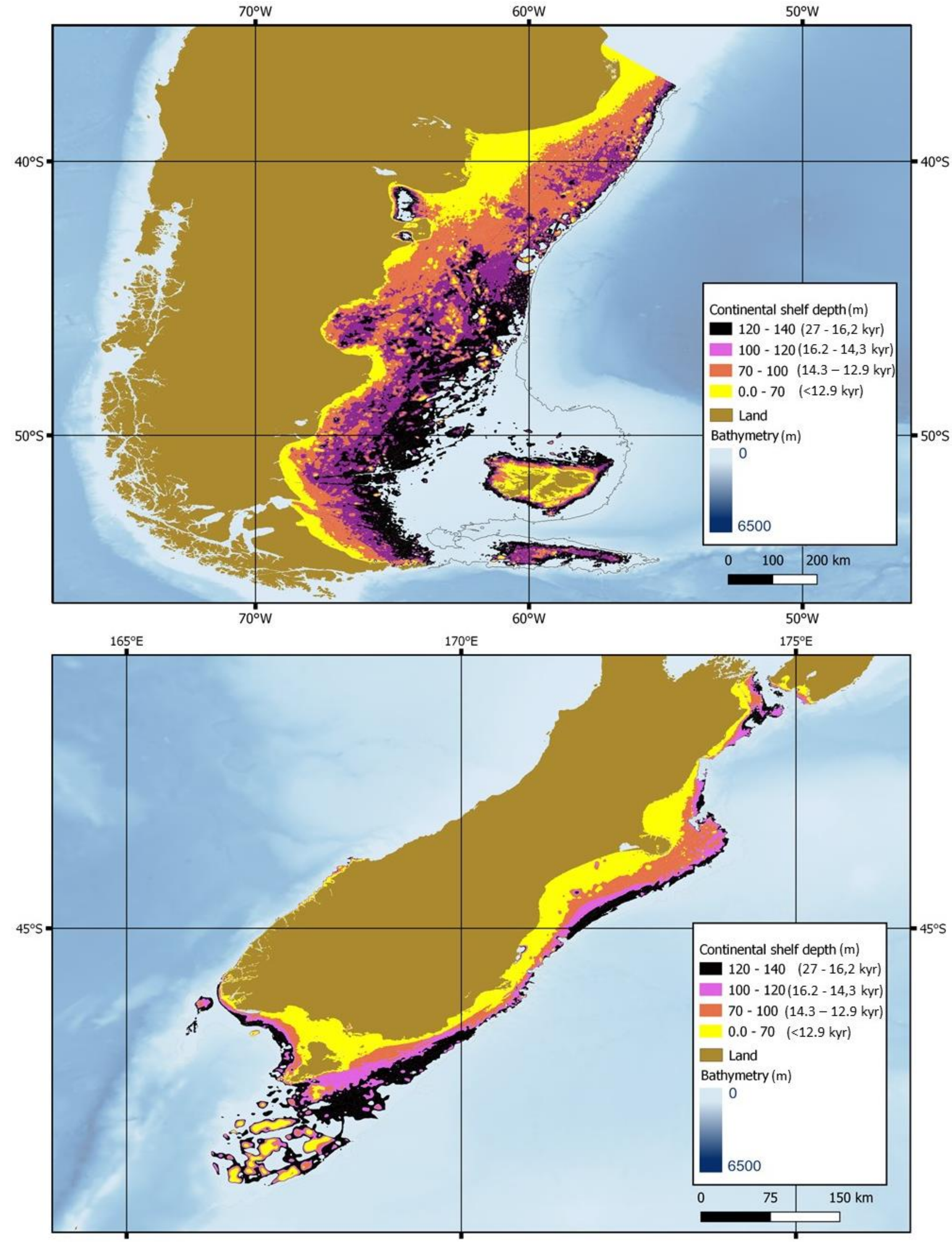

*Fig. S8: (**A** and **B**) Maps of emerged shelves in PAT and S-NZ over time through the LGIT. Black line in the -500 m contour lines. Different colors denote the shelves submerged from the maximum glacial low-stand up until 16.2 kyr (black), from 16.2 to 14.3 kyr, (purple), from 14.3 to 12.8 kyr (orange) and* *later than 12.8 kyr (yellow). Results of extended shelf surface area are similar to (17) for PAT and (16) for S-NZ.*